International Journal of
Molecular Sciences

MDPI

Article

Oxygen-Vacancy-Induced Electronic Structure Modulation in $ZnTiO_3$ Perovskite: A Combined DFT and SCAPS-1D Study Toward Photovoltaic Applications

Angel Tenezaca [1] and Ximena Jaramillo-Fierro [2,*]

[1] Carrera de Ingeniería Química, Universidad Técnica Particular de Loja, San Cayetano Alto, Loja 1101608, Ecuador; aptenezaca1@utpl.edu.ec
[2] Departamento de Química, Facultad de Ciencias Exactas y Naturales, Universidad Técnica Particular de Loja, San Cayetano Alto, Loja 1101608, Ecuador
* Correspondence: xvjaramillo@utpl.edu.ec; Tel.: +593-7-3701444

Abstract

Zinc titanate ($ZnTiO_3$) is a chemically stable and non-toxic oxide perovskite whose photovoltaic potential remains largely unexplored due to its wide indirect bandgap. This study evaluates whether oxygen-vacancy (F-center) engineering can tailor its electronic structure and improve its suitability as a photovoltaic absorber. Density Functional Theory (DFT) calculations using VASP (PAW − GGA/PBE + U) were performed to evaluate structural stability, electronic properties, and electron affinity, while optical absorption was modeled through a combined Tauc–Gaussian approach. Device performance was assessed via SCAPS-1D simulations in an FTO/ZnO/$ZnTiO_3$/Spiro-OMeTAD architecture. Oxygen vacancies induce bandgap narrowing from ~2.96 eV to ~1.47 eV and generate Ti-3d-dominated donor-like and deep intragap states. The calculated electron affinity is ~3.77 eV. Simulated single-layer devices reach Voc ≈ 1.11 V, Jsc ≈ 8.27 mA·cm^{-2}, FF ≈ 83%, and a maximum efficiency of ~7.65%, primarily limited by moderate absorption strength and defect-assisted recombination. Multilayer configurations indicate that geometric optimization can significantly enhance projected efficiency, approaching 19.25% under idealized conditions. Although vacancy engineering extends visible-light absorption, the intrinsic indirect band-gap character constrains the ultimate photovoltaic performance of $ZnTiO_3$.

Keywords: $ZnTiO_3$ perovskite; oxygen vacancies; density functional theory (DFT); SCAPS-1D simulation; perovskite oxides; bandgap narrowing; photovoltaic performance

Check for updates

Academic Editors: Aikaterini K. Andreopoulou, Elias Stathatos and Dimitris A. Chalkias

Received: 26 February 2026
Revised: 11 March 2026
Accepted: 13 March 2026
Published: 14 March 2026

Copyright: © 2026 by the authors. Licensee MDPI, Basel, Switzerland. This article is an open access article distributed under the terms and conditions of the Creative Commons Attribution (CC BY) license.

1. Introduction

Zinc titanate ($ZnTiO_3$) is an oxide perovskite of growing scientific and technological interest due to its chemical stability, non-toxic nature, photocatalytic activity, and tunable electronic structure enabled by defect engineering [1,2]. Compared to hybrid organic–inorganic perovskites, oxide perovskites exhibit superior structural robustness, making them promising platforms for sustainable optoelectronic applications [3,4]. In this context, perovskite-type $ZnTiO_3$ has been extensively explored as an electron transport layer (ETL) owing to its favorable band alignment and high optical transparency [5]. Nevertheless, this application reflects only part of its functional potential. A more comprehensive understanding of its defect-mediated electronic structure is therefore essential to fully assess its broader optoelectronic relevance.

Zinc titanate crystallizes in several polymorphs, including ilmenite, spinel, and perovskite-type phases, whose symmetry and atomic coordination strongly influence orbital hybridization, band scattering, and defect energetics [6]. $ZnTiO_3$ perovskite can adopt either hexagonal or cubic symmetry, which plays a decisive role in defining its electronic behavior. The cubic phase, characterized by greater symmetry, facilitates electron redistribution and can promote higher carrier mobility. Conversely, the hexagonal phase generally exhibits greater thermodynamic stability and lower susceptibility to structural collapse following the formation of an oxygen vacancy [6,7]. Overall, $ZnTiO_3$ perovskite behaves as a wide-bandgap nonmagnetic semiconductor with predominantly indirect transitions. The valence band (VB) is governed mainly by O-2p states, while the conduction band (CB) is dominated by Ti-3d orbitals, with additional contributions from Zn-3d states [8,9].

Intrinsic point defects, particularly oxygen vacancies, critically influence the electronic response of oxide perovskites, including $ZnTiO_3$. Neutral oxygen vacancies (F-centers) introduce localized states within the bandgap and modify charge redistribution, symmetry, and electrostatic alignment [10]. Depending on their energetic position and orbital hybridization, these states may act as shallow donor-like levels that increase carrier density or as deep traps that promote non-radiative recombination [7]. In titanate systems, vacancy formation is often accompanied by Ti-centered electronic localization. This process leads to band-gap renormalization and defect-induced optical absorption [11]. Consequently, oxygen-vacancy control provides a strategy for tuning the photophysical properties of $ZnTiO_3$. However, this strategy increases the complexity of device optimization and requires computational methods capable of resolving defect–electronic interactions with atomic precision [12].

From an optical perspective, absorption in $ZnTiO_3$ has traditionally been described using Tauc-based models combined with Gaussian functions to represent sub-gap states associated with intrinsic defects or structural disorder [2]. These models reproduce macroscopic spectral features, including indirect absorption-slopes and Urbach tails. However, they do not fully capture electronic transitions mediated by O-2p and Ti-3d interactions or the redistribution of defect-induced states in wide-bandgap systems [13]. This limitation highlights the need to complement classical optical models with ab initio electronic-structure calculations that explicitly account for vacancy-induced orbital modulation.

Recent advances in perovskite solar cell (PSC) research have shown that computational tools such as VASP and SCAPS provide powerful frameworks for linking fundamental material properties to device-level performance. Density Functional Theory (DFT) enables the evaluation of structural stability, free energies, density of states, and defect energetics with a level of resolution that is difficult to achieve experimentally [14]. SCAPS has become a standard platform for one-dimensional photovoltaic modeling. It allows the assessment of charge transport, trap densities, band alignment, and interfacial effects in multilayer architectures [15,16]. Even in DFT may underestimate bandgaps [17] and drift–diffusion simulations involve geometric idealizations [14], the combined use of these methods provides a coherent structure–property–function framework for emerging photovoltaic materials.

Although PSC technologies have reached efficiencies comparable to crystalline silicon, large-scale deployment remains limited by long-term instability and lead toxicity [18]. These challenges motivate the exploration of stable inorganic alternatives, including oxide-based perovskites. However, a comprehensive molecular-level analysis that integrates structural phase stability, oxygen-vacancy energetics, orbital-resolved electronic states, vacuum-level alignment, and device-relevant parameters has not yet been systematically developed for $ZnTiO_3$. In particular, the extent to which vacancy-induced bandgap nar-

rowing and Ti-3d state redistribution modify electron affinity, optical absorption, and macroscopic photovoltaic response remains insufficiently clarified.

In this study, oxygen vacancy-induced modulation of the electronic structure in perovskite-like $ZnTiO_3$ was investigated using first-principles DFT calculations combined with one-dimensional photovoltaic simulations. Phase stability, vacancy stabilization energies, orbital-resolved density of states, band-gap renormalization, and electrostatic alignment were analyzed. The results elucidate how neutral F centers redistribute Ti-3d-derived states and reshape the electronic landscape. The resulting electronic parameters were incorporated into SCAPS simulations to evaluate their impact on photovoltaic performance in an FTO/ZnO/$ZnTiO_3$/Spiro-OMeTAD architecture. This integrated approach provides molecular-level insight into defect physics in $ZnTiO_3$ and clarifies its realistic potential within emerging oxide-based photovoltaic materials.

2. Results and Discussion

2.1. Structural Optimization of $ZnTiO_3$

Structural optimization of $ZnTiO_3$ was performed in the cubic and hexagonal phases to establish a consistent reference frame before electronic and optical analyses. The cubic supercell of $ZnTiO_3$ (Figure 1a) converged to lattice parameters of a = b = c = 11.58 Å and angles $\alpha = \beta = \gamma = 90^\circ$, while the hexagonal phase was modeled using its crystallographically equivalent trigonal representation (Figure 1b), which offers a compact, symmetry-preserving description of the lattice without compromising structural fidelity. This choice is supported by previous studies demonstrating that the R-3 hexagonal phase can be rigorously mapped onto a rhombohedral/trigonal lattice [8,19] whose supercell relaxed to a = 14.86 Å, b = 20.59 Å, c = 6.50 Å, with angles $\alpha = \beta = 90^\circ$ and $\gamma = 99.9763^\circ$ [20].

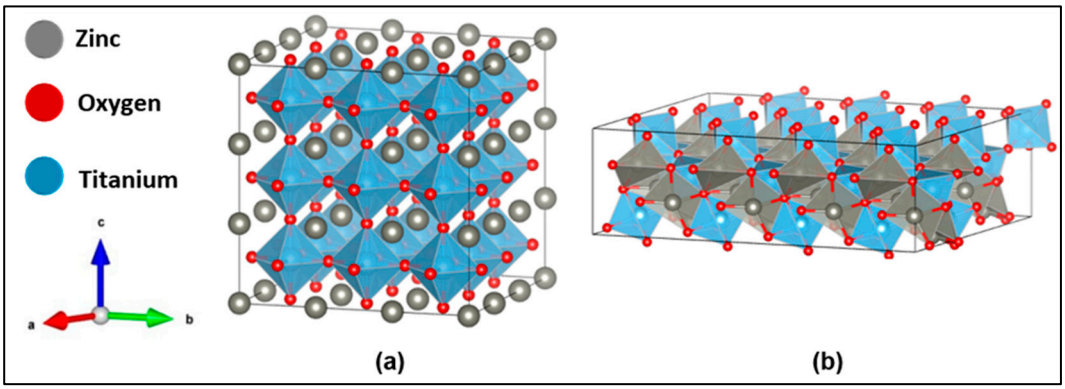

Figure 1. Optimized structures of supercells of $ZnTiO_3$: (**a**) cubic and (**b**) hexagonal.

The fractional atomic coordinates of the cubic and hexagonal $ZnTiO_3$ supercells are presented in Tables S1 and S2, respectively. On the other hand, Table S3 presents the total free energies obtained for bulk and slab configurations of $ZnTiO_3$ in the hexagonal and cubic phases after full structural relaxation. These values serve as a reference for comparing the relative stability of the models considered. For the cubic phase, only bulk and pristine slab configurations are reported, exhibiting higher total free energies than their hexagonal counterparts. On this basis, the hexagonal structure was selected as the reference phase for the defect analysis and for the electronic, optical, and device-level simulations discussed in the main text.

The surface models presented in Figure 2 were constructed from the optimized supercells shown in Figure 1 by cleaving the bulk along the (101) crystallographic plane and periodically extending the slab in the in-plane directions to generate equivalent surfaces for the cubic and hexagonal polymorphs of $ZnTiO_3$. Each slab consisted of three

atomic layers and included a 15 Å vacuum region along the surface normal to suppress false interactions between periodic images and to ensure an unambiguous reference for electrostatic potential.

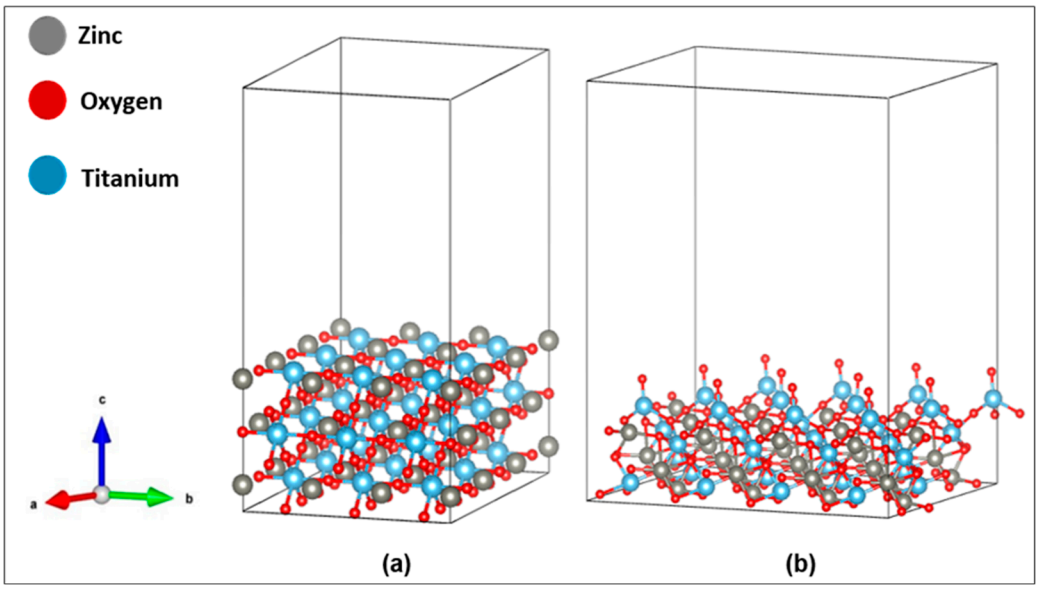

Figure 2. Optimized structures of plane (101) of $ZnTiO_3$ perovskite: (**a**) cubic and (**b**) hexagonal.

The decision to investigate only the (101) plane is based on thermodynamic and application-relevant considerations, as several DFT studies have shown that the (101) facet exhibits the lowest surface energy among the accessible terminations of structures derived from $ZnTiO_3$ and related titanates, and is therefore considered the most stable and representative surface under ambient or near-ambient conditions [20]. Therefore, this study does not re-evaluate the stability of $ZnTiO_3$ surfaces; instead, it focuses on the electronic and defect-related properties of the most well-supported stable (101) slab, quantifying its response to oxygen-vacancy formation and assessing its relevance for device-level band alignment.

2.2. Determination of Electronic Properties of $ZnTiO_3$

Table 1 compiles reported cases of bandgap reduction in the range of titanates and oxides following the introduction of oxygen vacancies (VO). These values provide a baseline overview that helps anticipate the degree to which $ZnTiO_3$ might be affected under comparable defect conditions. For each compound, the table contrasts the pristine bandgap with the value obtained after VO creation, highlighting the characteristic narrowing observed across different systems. In this context, only neutral oxygen vacancies (referred to as F centers) are considered, as they represent the most physically stable defect state and are widely reported under intrinsic or near-stoichiometric conditions [2,6,7]. Charged vacancies are highly dependent on the Fermi-level position, extrinsic doping, and specific electrochemical environments, introducing additional variables that complicate direct comparison between different materials [21].

From the data summarized in Table 1, the average band-gap reduction induced by the neutral oxygen vacancies in titanates and related oxides is approximately 1.09 eV, with reported values ranging from 0.70 to 1.50 eV. This range reflects the vacancy-driven band-gap reduction obtained for $ZnTiO_3$ in this study, with the gap narrowing from 2.96 eV to ~1.48 eV (Table 2), yielding $\Delta E \approx 1.48$ eV. This confirms that the defect-induced electronic restructuring observed here is within the expected physical regime for oxide perovskites, thus validating the use of obtained values.

Table 1. Modification of bandgap energy (E_g) due to F-centers.

Compound	E_g Original (eV)	E_g with VO (eV)	Difference ΔE	Reference
Lead Titanate	3.200	2.360	0.840	[11]
Barium Titanate	1.787	1.000	0.787	[22]
Strontium Titanate	3.200	1.895	1.305	[23]
Calcium Titanate	3.550	2.050	1.500	[24]
Anatase (TiO_2)	3.100	1.940 − 1.500	1.160	[25]
Zinc Oxide (ZnO)	3.200	2.500	0.700	[26]

From the data summarized in Table 1, the average band-gap reduction induced by the neutral oxygen vacancies in titanates and related oxides is approximately 1.09 eV, with reported values ranging from 0.70 to 1.50 eV. This range reflects the vacancy-driven band-gap reduction obtained for $ZnTiO_3$ in this study, with the gap narrowing from 2.96 eV to ~1.48 eV (Table 2), yielding $\Delta E \approx 1.48$ eV. This confirms that the defect-induced electronic restructuring observed here is within the expected physical regime for oxide perovskites, thus validating the use of obtained values.

Table 2. Effect of the F-center on electronic levels and bandgap.

Structure	Fermi Level (eV)	Conduction Band Level (eV)	Valence Band Level (eV)	Bandgap (eV)
$ZnTiO_3$ without vacancy	3.098	1.661	−1.296	2.957
* $ZnTiO_3$–slab 101 with one vacancy	−2.884	0.780	−0.695	1.475

* The electronic levels of the slab with a vacancy include the dipolar plateau correction.

In the defect-free case, (Figure 3a) the DOS exhibits a well-defined forbidden region with no electronic states within the bandgap, which is consistent with the wide-gap semiconductor nature of $ZnTiO_3$. Following the introduction of oxygen vacancies (Figure 3b), the DOS profile is characterized by an apparent narrowing of the bandgap and the appearance of localized intragap states. These intragap features originate from F centers associated with the oxygen vacancies [27] and perform two electronic roles. States located near the conduction band minimum act as surface donor levels, effectively supplying free electrons and facilitating n-type conductivity. Conversely, deeper states, located farther from the band edges, behave as deep traps, capturing charge carriers and acting as recombination centers [28]. This differentiation between donor-like states and deep traps is fundamental, as it explains why oxygen vacancies simultaneously enhance optical absorption through narrowing of the bandgap and, at the same time, introduce recombination pathways that can limit the carrier's lifetime if its density becomes excessive.

In the present study, the density-of-states analysis reveals that the electronic states induced by the vacancy are predominantly located near the conduction band. This energetic positioning indicates that oxygen vacancies in $ZnTiO_3$ primarily exhibit donor-like behavior under neutral charge conditions, effectively contributing electrons to the conduction band. As shown in the total (Figure 4a) and partial DOS, the valence-band region is predominantly governed by O-2p states with additional hybridization from Zn-3d orbitals, while the conduction-band edge is largely dominated by Ti-3d states, which agrees with previous electronic-structure analyses of $ZnTiO_3$ [20]. It is evident that removing the oxygen suppresses the O-2p contribution near the valence-band edge (Figure 4b) and increases the Ti-3d weight near the conduction-band minimum. This occurs because the excess electrons released by the oxygen vacancy are accommodated in Ti-centered states [7]. The

partial DOS bandgap (Figure 4c) is predominantly governed by Ti-3d contributions. Near the conduction-band edge, Ti-3d-derived states are energetically shallow and delocalized, behaving as donor-like levels, thereby increasing the availability of electrons for n-type conduction [29]. At lower energies within the gap, Ti-3d states become progressively more localized, with reduced hybridization with O-2p orbitals, resulting in deep features within the gap that act as efficient carrier trapping and recombination centers [29]. The absence of significant contributions derived from Zn near the conduction-band edge (Figure 4d) further confirms the secondary electronic role of Zn in carrier transport, reinforcing that the vacancy-driven electronic restructuring is primarily mediated by the Ti–O sublattice [6].

The electronic band structure calculated along the high-symmetry Γ–M–K path (Figure 5a) provides further insight into the defect-mediated electronic behavior of $ZnTiO_3$. The adoption of a two-dimensional (2D) reference path within the basal plane of the Brillouin zone is justified by the hexagonal/ilmenite-like symmetry of the stabilized phase, for which the most relevant band ends and dispersion features are captured by k-space directions [30]. As evidenced in Figure 5b, the material exhibits an indirect band-gap transition, with the valence-band maximum located at the Γ region and the conduction-band minimum shifted toward the M/K region, resulting in an effective bandgap of approximately 1.47–1.48 eV; this value is consistent with that previously obtained by the density-of-states (DOS) analysis. Furthermore, the appearance of nearly flat bands within the forbidden gap, characterized by low k-dispersion, indicates the presence of highly localized defect states (deep traps) [29]. Conversely, the bands forming the edge of the conduction-band display a higher dispersion, indicating lower effective electron masses and higher carrier mobility, which supports the donor-like role of oxygen vacancies inferred from the DOS results [8]. Overall, the coexistence of dispersive conduction states and localized intragap levels, induced by oxygen vacancies, simultaneously causes an improvement in electron mobility and Shockley–Read–Hall Recombination (SRH), which affect photovoltaic efficiency [29].

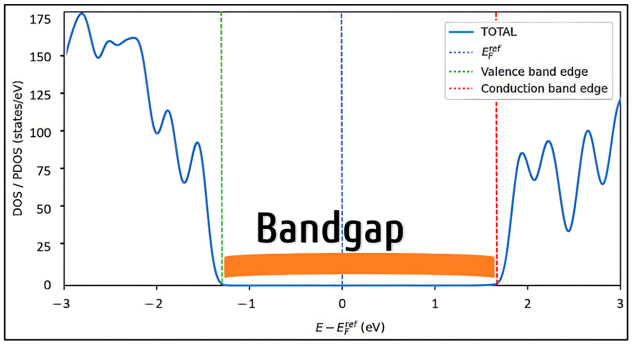

(**a**)

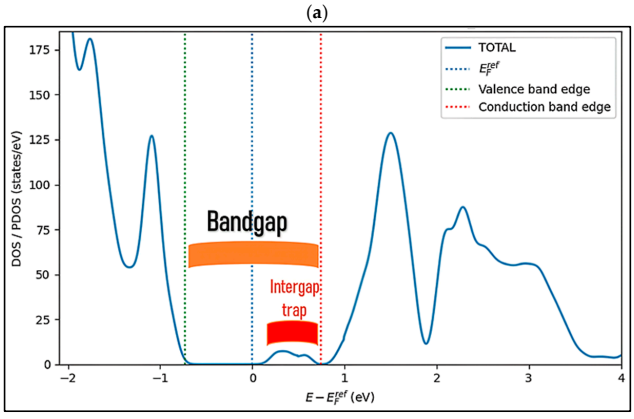

(**b**)

Figure 3. Density of states (DOSs) of $ZnTiO_3$: (**a**) without vacancies and (**b**) with vacancies.

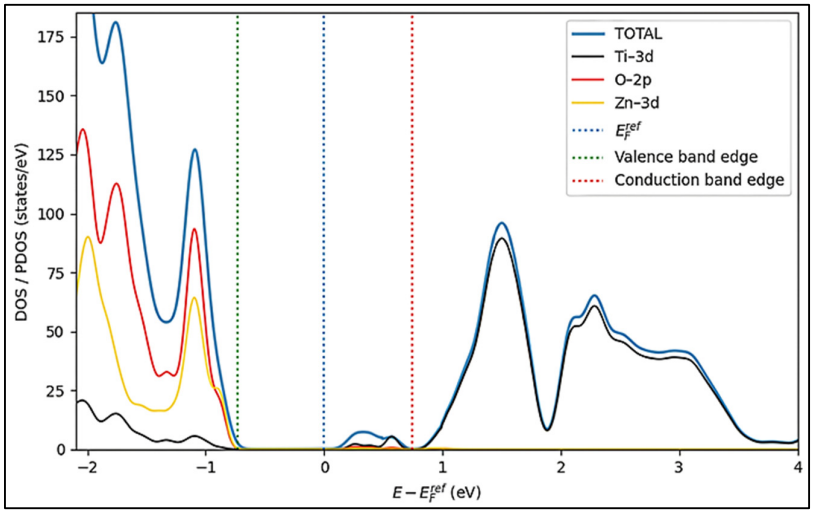

(**a**)

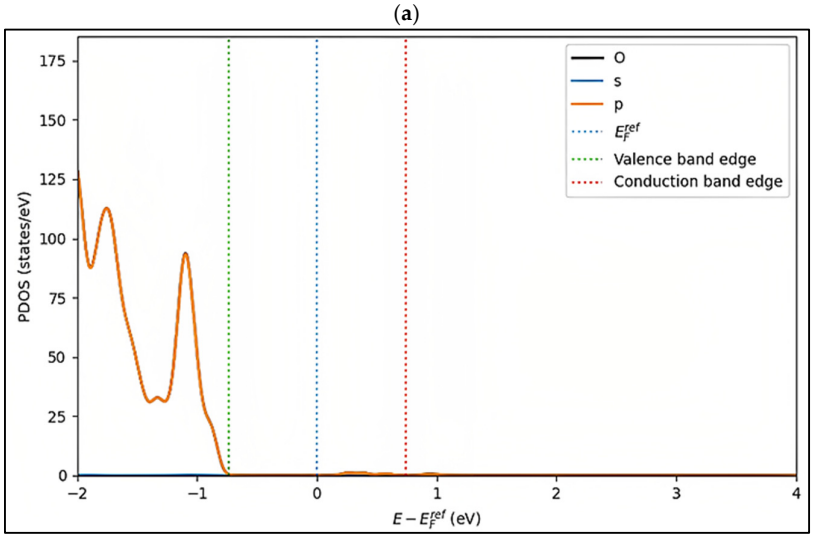

(**b**)

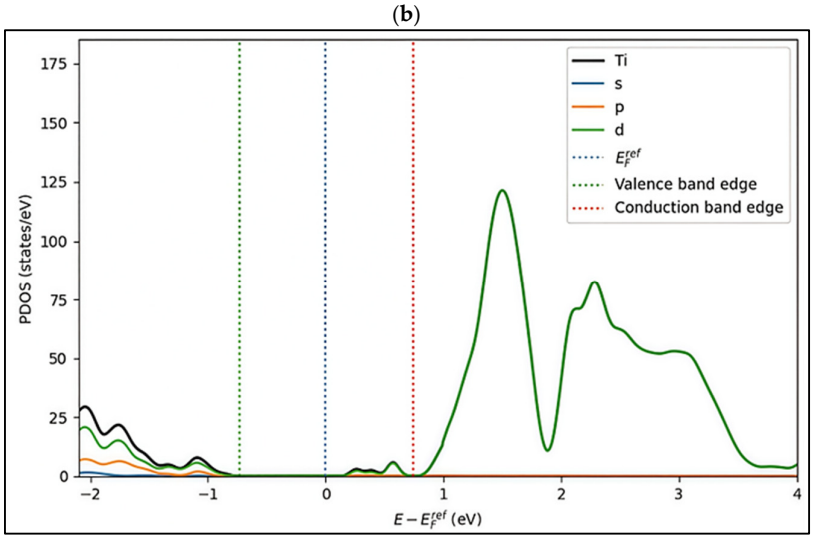

(**c**)

Figure 4. *Cont.*

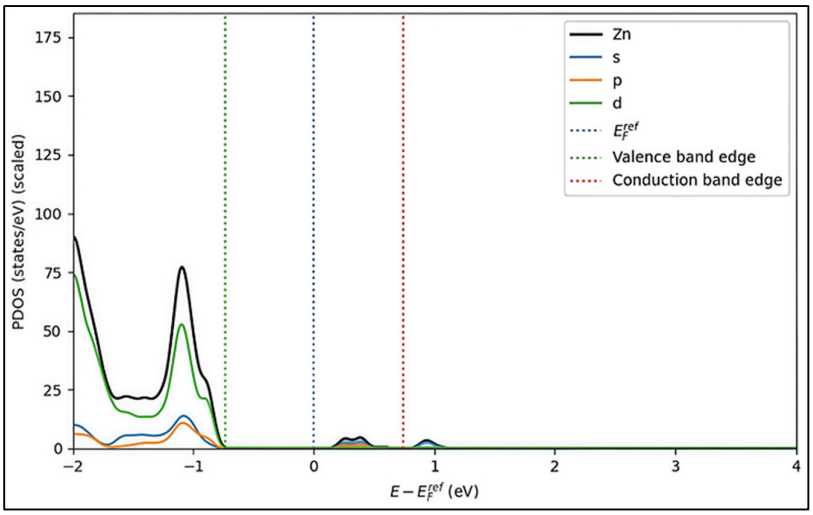

(**d**)

Figure 4. Density of states (DOSs) of $ZnTiO_3$: (**a**) total and partial of (**b**) O, (**c**) Ti and (**d**) Zn.

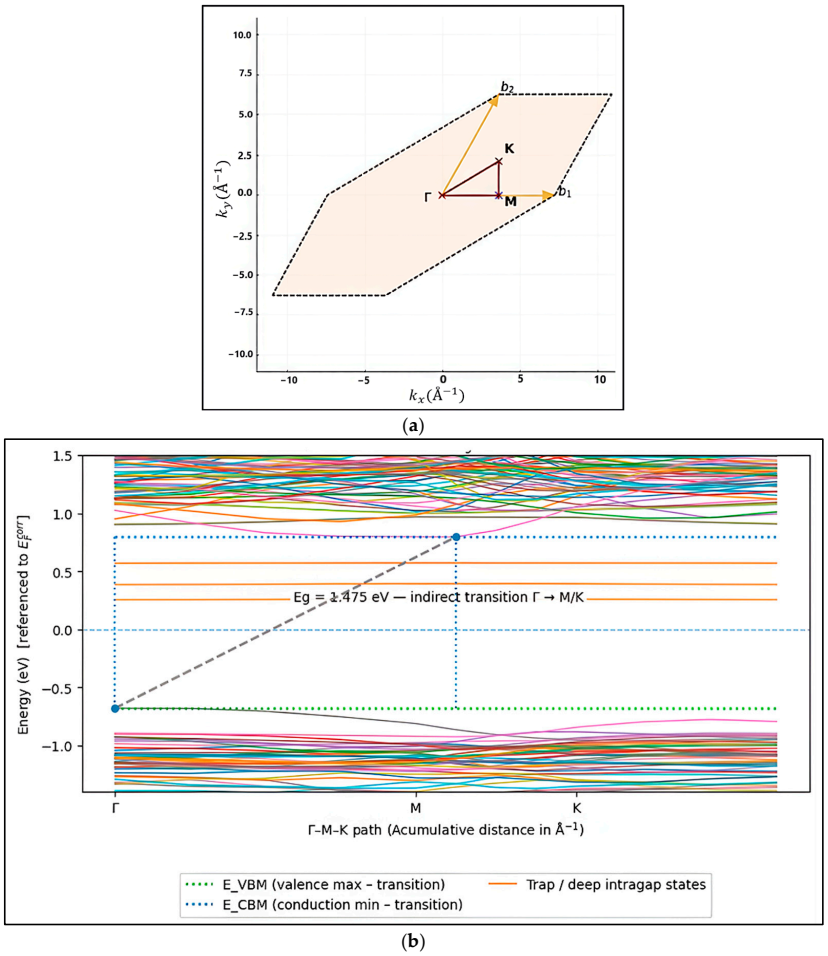

(**a**)

(**b**)

Figure 5. (**a**) Two-dimensional representation of the first Brillouin zone for the hexagonal primitive cell used in the band structure calculation, with high-symmetry k-points (Γ, M and K) and the corresponding reciprocal vectors indicated (b_1 and b_2). (**b**) Band structure of $ZnTiO_3$ along the high-symmetry Γ–M–K path in the first Brillouin zone.

2.3. Determination of the Absorption Model of $ZnTiO_3$ Perovskite

Density-of-states and band structure analyses demonstrate that F centers generate both donor-like Ti-3d states and deeper, localized intragap states [7]. This lowers the energy

threshold for allowed optical transitions, extending the absorption edge into the visible spectral range [31]. However, despite the theoretical evidence supporting defect-induced absorption in perovskites and mixed oxides [32], direct experimental determination of the absorption coefficient for $ZnTiO_3$ under controlled oxygen-vacancy concentrations is limited. Most experimental studies on $ZnTiO_3$ have focused on photocatalytic performance, dielectric properties, or optical transparency in the UV region, without addressing the contribution of vacancy-induced subgap states to visible-light absorption [3]. In the absence of experimental evidence indicating that oxygen vacancies significantly enhance the absolute magnitude of the absorption coefficient, the optical response of $ZnTiO_3$ (plus vacancies) was conservatively set at the absorption level reported for pristine $ZnTiO_3$ ($\alpha \approx 10^4$ cm^{-1}) [31], while the vacancy-induced bandgap narrowing regulates the shift in the absorption onset. Consequently, the absorption model adopted in this study is based on electronic structure DFT calculations to establish a physically consistent optical response.

Comparison with the hybrid halide perovskite $CH_3NH_3PbI_3$, currently considered the reference absorber for high-efficiency perovskite solar cells, provides further physical insight into the implications of the obtained absorption model. As shown in Figure 6, the hybrid perovskite exhibits absorption coefficients on the order of 10^5 cm^{-1} across most of the visible spectrum, while $ZnTiO_3$ shows values approximately an order of magnitude lower. This pronounced difference arises from the distinct optical mechanisms governing each material: in hybrid perovskites, strong absorption originates from direct bandgap transitions and highly dispersive band edges [2]. In contrast, $ZnTiO_3$ retains an indirect bandgap character even after vacancy-induced narrowing, which intrinsically limits transition probabilities and reduces the absorption strength [6]. This comparison shows that $ZnTiO_3$ (enhanced with defect engineering) does not achieve absorption levels comparable to those of hybrid perovskites, but it offers superior stability, a non-toxic composition, and an adjustable electronic structure. Therefore, rather than competing with hybrid perovskites solely in terms of optical power, $ZnTiO_3$ is better suited for use as a complementary absorber or in tandem and multilayer architectures, where these characteristics can be leveraged to improve the overall performance of the device.

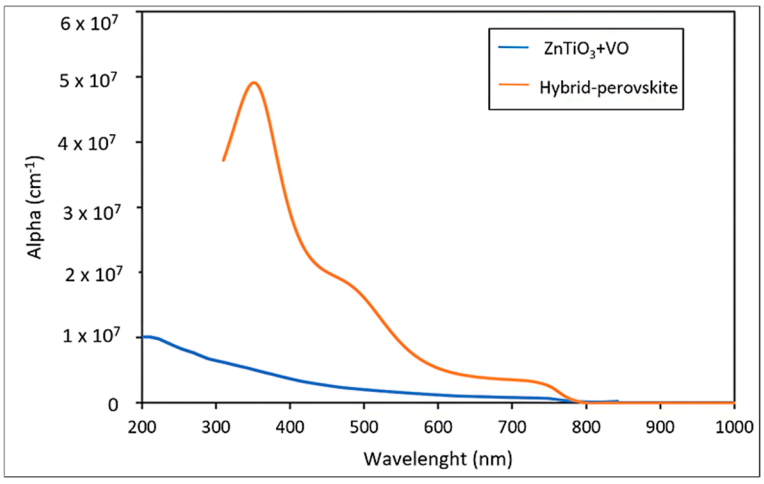

Figure 6. Optical absorption curves of $ZnTiO_3$ perovskite and hybrid-perovskite ($CH_3NH_3PbI_3$).

2.4. Analysis of Photovoltaic Performance of $ZnTiO_3$ with F-Centers Using SCAPS-1D

The photovoltaic performance of $ZnTiO_3$ was evaluated in a standard perovskite-type solar cell architecture using the SCAPS-1D numerical simulator. The objective of this analysis was to establish a baseline evaluation of the photovoltaic behavior of $ZnTiO_3$ as an absorber layer, rather than seeking exhaustive optimization of the device configuration.

Therefore, a conventional FTO/ZnO/$ZnTiO_3$/Spiro-OMeTAD structure was adopted, employing electron and hole transport layers, which are widely used in perovskite solar cells and whose electronic properties are well documented in the literature [33]. This choice allows the role of $ZnTiO_3$ within a reproducible framework, while minimizing the influence of factors such as advanced interface engineering or material-specific optimization strategies, which are outside the scope of this initial study.

The physical and electronic parameters assigned to each layer, including thickness, bandgap, electron affinity, dielectric permittivity, effective density of states, carrier mobilities, and doping concentrations, are summarized in Table 3. These values were chosen based on previously determined electronic properties for $ZnTiO_3$ and on parameter sets commonly reported for Fluorine-doped tin oxide (FTO), ZnO, and Spiro-OMeTAD in SCAPS-based simulations of perovskite solar cells [16]. For the $ZnTiO_3$ absorber, the modeled defects do not explicitly correspond to oxygen vacancies but rather represent generic bulk defect states distributed throughout the material that can act as surface or deep recombination centers, consistent with the electronic structure analysis discussed in the previous sections [16,28]. Only SRH recombination was considered in the present simulations. Radiative recombination was ruled out due to the indirect bandgap of $ZnTiO_3$, whose radiative transitions are weak and do not dominate carrier losses under standard operating conditions [34]. Auger recombination, although potentially relevant at very high carrier densities [29], was not included to avoid unnecessary model complexity and additional fitting parameters. While its inclusion could increase the realism of the simulation, it would divert attention from the main objective of this study, which is to provide a practical and physically consistent estimate of the expected photovoltaic performance of $ZnTiO_3$.

Table 3. Input parameters in SCAPS for each layer of the PSC.

Parameter	FTO [35,36]	ZnO (ETL) [33]	$ZnTiO_3$	Spiro-OMeTAD (HTL) [36]
Thickness (nm)	500	50	300	100
Bandgap E_g (eV)	3.5	2	1.475	3.00
Electron affinity χ (eV)	4.0	4.00	3.770	2.45
Dielectric permittivity (ε_r)	9.0	9.0	10.50	3.00
Effective density of states in CB, N_c (cm^{-3})	2.2×10^{18}	3.7×10^{18}	2.2×10^{18}	2.2×10^{18}
Effective density of states in BV, N_v (cm^{-3})	1.8×10^{19}	1.8×10^{19}	1.8×10^{19}	1.8×10^{19}
Thermal velocity of electrons ($cm\ s^{-1}$)	1.0×10^{7}	1.0×10^{7}	1.0×10^{7}	1.0×10^{7}
Thermal velocity of holes ($cm\ s^{-1}$)	1.0×10^{7}	1.0×10^{7}	1.0×10^{7}	1.0×10^{7}
Electron mobility, μ_n ($cm^2\ V^{-1}\ s^{-1}$)	20	100	2.5	2×10^{-4}
Hole mobility, μ_p ($cm^2\ V^{-1}\ s^{-1}$)	10	25	1.0	2×10^{-4}
Donor density, N_D (cm^{-3})	2.0×10^{19}	5.0×10^{17}	Variable	0
Acceptor density, N_A (cm^{-3})	0	0	0	2.0×10^{18}

Figure 7 illustrates the device configurations considered for the SCAPS simulations. The single-layer structure shown in Figure 7a represents the physically feasible reference model, in which $ZnTiO_3$ is considered a homogeneous absorber layer. In contrast, the multilayer configuration depicted in Figure 7b corresponds to a hypothetical construct introduced to explore the effect of spatially distributed defect populations and varying donor–trap ratios along the absorber thickness.

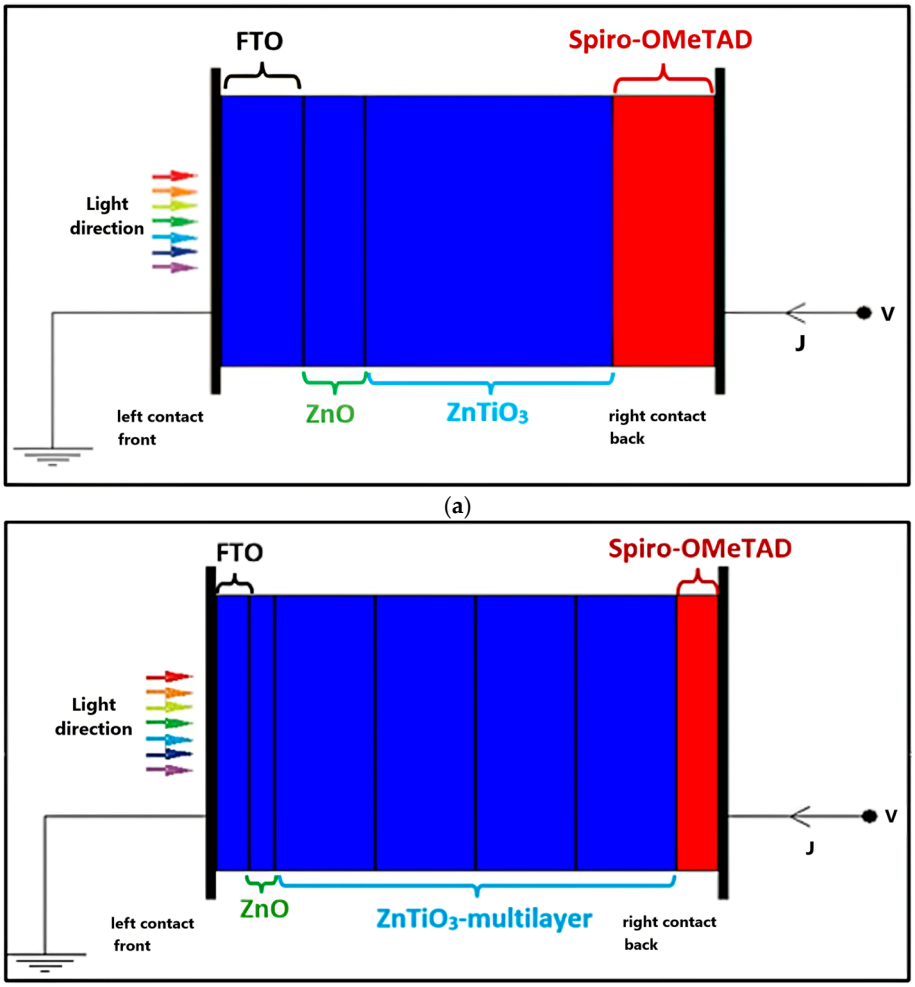

Figure 7. Scheme of $ZnTiO_3$-type perovskite solar cell: (**a**) single-layer (feasible model) and (**b**) multilayer (hypothetical model). In the figure, blue layers represent n-type regions, and the red layers represent p-type regions. Besides, V denotes the applied voltage at the back contact, while J represents the current density flowing through the device.

The configuration shown in Figure 7 is not intended to reproduce a viable manufacturing route but rather serve as a numerical framework for examining how different defect fractions influence carrier screening, recombination behavior, and overall device performance. Based on this approach, the volumetric densities of deep trap states and donor-like states were systematically varied according to the relative fraction of oxygen vacancies, as summarized in Table 4. For each vacancy concentration, the total effective defect density N_t was kept constant, while the relative contribution of the deep traps and donor states was adjusted. This allows for a clearer interpretation of how the donor–trap equilibrium governs the electrostatic sensing length and recombination dynamics within the absorber.

The Debye length L_D provides a direct measure of the length of electrostatic shielding within the absorber and is therefore a key criterion for device stability. To maintain an effective electric field in the depletion region, the absorber thickness z must be several times greater than the Debye length, thus satisfying the empirical condition: $L_D < \frac{z}{5}$, which means that the L_D must remain below approximately 15–25% of the total thickness [37,38].

Table 4. Volumetric densities of deep traps and donor states as function of relative fractions for different oxygen vacancy concentrations.

Vacancies Fraction θ_{VO} (%)	Deep Trap Fraction θ_{tr}	Donor Fraction θ_D	Deep Trap Density N_{tr} (cm^{-3})	Donor Density N_D (cm^{-3})	Debye Length L_D (nm)
0.1 (1 VO for every 1000 crystal sites) $N_{t,eff}$ (cm^{-3}) = 1.77×10^{16}	0.5	0.5	8.85×10^{15}	8.85×10^{15}	41.18
	0.4	0.6	7.08×10^{15}	1.06×10^{16}	37.59
	0.3	0.7	5.31×10^{15}	1.24×10^{16}	34.80
	0.2	0.8	3.54×10^{15}	1.42×10^{16}	32.56
	0.1	0.9	1.77×10^{15}	1.59×10^{16}	30.69
0.05 (1 VO for every 5000 crystal sites) $N_{t,eff}$ (cm^{-3}) = 8.85×10^{15}	0.5	0.5	4.43×10^{15}	4.43×10^{15}	58.24
	0.4	0.6	3.54×10^{15}	5.31×10^{15}	53.16
	0.3	0.7	2.66×10^{15}	6.20×10^{15}	49.22
	0.2	0.8	1.77×10^{15}	7.08×10^{15}	46.04
	0.1	0.9	8.85×10^{14}	7.97×10^{15}	43.41
0.01 (1 VO for every 10,000 crystal sites) $N_{t,eff}$ (cm^{-3}) = 1.77×10^{15}	0.5	0.5	8.85×10^{14}	8.85×10^{14}	130.22
	0.4	0.6	7.08×10^{14}	1.06×10^{15}	118.88
	0.3	0.7	5.31×10^{14}	1.24×10^{15}	110.06
	0.2	0.8	3.54×10^{14}	1.42×10^{15}	102.95
	0.1	0.9	1.77×10^{14}	1.59×10^{15}	97.06

Experimental depth profiling studies in perovskite oxides and related oxide semiconductors indicate that vacancy redistribution and near-surface electrostatic effects typically extend to several tens of nanometers from the surface [39], defining a near-surface defect-modulated region. Similarly, space charge layer widths in $SrTiO_3$-based defective systems have been reported to range from tens to hundreds of nanometers, depending on the doping level and thermodynamic conditions [40]. Considering these experimentally observed spatial scales, an absorber thickness of approximately 250–300 nm was selected. This range ensures that the vacancy-affected domain near the surface is fully contained, while allowing the remaining portion of the film to approach bulk-like behavior. Beyond 300 nm, the exponential decay of defect concentration progressively reduces donor states and deep traps to marginal levels, typically well below 0.01% of the surface value, such that $ZnTiO_3$ progressively approaches bulk-like behavior and vacancy-induced visible absorption is effectively suppressed [7].

It should be noted that determining the exact characteristic thickness of the evaluated material lies beyond the scope of this study. Therefore, the values adopted are considered a physical reference scale, based on experimentally reported magnitudes in comparable oxide systems. Under this configuration, satisfying the empirical electrostatic condition of the total thickness implies a characteristic shielding length on the order of 30–60 nm. This leads to the adoption of a representative decay length of 50 nm for the spatial distribution of vacancy-induced perturbations. It is worth highlighting that, although the present DFT calculations consider neutral oxygen vacancies (F-centers), the characteristic length adopted here reflects the spatial scale at which defect-induced electronic perturbations and electrostatic shielding effects coexist in the device environment.

Following the criterion, Debye lengths below $\leq$50 nm were identified as the desirable regime, as they allow adequate penetration of the internal electric field maintaining efficient carrier transport and defect-assisted optical absorption [41]. As shown in Table 4, this condition is only met in donor-dominated configurations with vacancy fractions of 0.10% and 0.05%, where the Debye length (L_D) remains in the range of ~31–49 nm depending on the relative balance between donor states and deep traps. Conversely, a vacancy fractions of 0.01% produce Debye lengths well above this threshold, indicating an over-screened regime in which electrostatic field penetration is strongly suppressed and device performance

becomes electrostatically limited. For this reason, the configuration with θvo = 0.01% was not considered in the photovoltaic simulations summarized in Table 5, since such conditions would lead to electrostatically limited device operation rather than a representative working regime of the absorber layer.

Table 5. Analysis of photovoltaic cell performance as a function of vacancy percentage and donor-trap fractions. θ_{VO}: oxygen-vacancy fraction; θ_{tr}: deep-trap fraction; θ_D: donor fraction; N_{tr}: deep-trap density; N_D: donor density; Voc: open-circuit voltage; Jsc: short-circuit current density; FF: fill factor; η: power conversion efficiency.

θ_{VO} (%)	θ_{tr}	θ_D	N_{tr} (cm^{-3})	N_D (cm^{-3})	V_{oc} (V)	J_{sc} ($\frac{mA}{cm^2}$)	FF (%)	η (%)
0.05	0.9	0.1	7.97×10^{15}	88.85×10^{14}	1.0999	8.268539	83.63	7.61
	0.7	0.3	6.20×10^{15}	2.66×10^{15}	1.1029	8.268556	83.48	7.61
	0.6	0.4	5.31×10^{15}	3.54×10^{15}	1.1045	8.268564	83.40	7.62
	0.5	0.5	4.43×10^{15}	4.43×10^{15}	1.1063	8.268572	83.33	7.62
	0.4	0.6	3.54×10^{15}	5.3×10^{15}	1.1081	8.268580	83.26	7.63
	0.3	0.7	2.66×10^{15}	6.20×10^{15}	1.1101	8.268588	83.18	7.64
	0.1	0.9	8.85×10^{14}	7.97×10^{15}	1.1146	8.268605	82.98	7.65
0.07	0.9	0.1	1.06×10^{16}	1.18×10^{15}	1.114	8.268514	83.82	7.60
	0.7	0.	8.26×10^{15}	3.54×10^{15}	1.0997	8.268536	83.65	7.61
	0.6	0.4	7.08×10^{15}	4.72×10^{15}	1.1017	8.268547	83.55	7.61
	0.5	0.5	5.90×10^{15}	5.90×10^{15}	1.1037	8.268558	83.45	7.62
	0.4	0.6	4.72×10^{15}	7.08×10^{15}	1.1059	8.268569	83.36	7.62
	0.3	0.7	3.54×10^{15}	8.26×10^{15}	1.1083	8.26858	83.27	7.63
	0.1	0.9	1.18×10^{15}	1.06×10^{16}	1.1139	8.268602	83.03	7.65
0.10	0.9	0.1	1.59×10^{16}	1.77×10^{15}	1.0918	8.268458	84.07	7.59
	0.7	0.3	1.24×10^{16}	5.31×10^{15}	1.0943	8.268496	83.92	7.59
	0.6	0.4	1.06×10^{16}	7.08×10^{15}	1.0967	8.268513	83.81	7.60
	0.5	0.5	8.85×10^{16}	8.85×10^{15}	1.0994	8.268529	83.68	7.61
	0.4	0.6	7.08×10^{16}	1.06×10^{16}	1.1022	8.268545	83.55	7.61
	0.3	0.7	5.31×10^{15}	1.24×10^{16}	1.1053	8.268562	83.41	7.62
	0.1	0.9	1.77×10^{15}	1.59×10^{16}	1.1127	8.268595	83.11	7.65

The photovoltaic behavior of the device as a function of the vacancy percentage and the relative fractions of the donor and trap states are shown in Table 5. Across all the tested vacancy concentrations and donor–trap ratios, the short-circuit current density (J_{sc}) exhibits negligible variation, indicating that the photocurrent is primarily governed by the intrinsic optical absorption of $ZnTiO_3$ and is largely insensitive to changes in the defect distribution within the explored range [16]. In contrast, the open-circuit voltage (V_{oc}) shows a clear dependence on the donor–trap balance. Configurations characterized by higher donor-state fractions yield improved voltage output, which can be attributed to a reduction in non-radiative losses governed by Shockley–Read–Hall (SRH) recombination, resulting in longer effective carrier lifetimes and a reduced recombination rate under open-circuit conditions [42]. The fill factor (FF) exhibits moderate variations as the defect distribution changes; this produces changes in carrier transport efficiency, along with variations in the effective strength of SRH recombination within the absorber layer [28]. Deep-level defects enhance carrier capture and recombination, increasing resistive losses and altering the shape of the current–voltage curve [38], while donor-dominated configurations enhance electrostatic shielding and charge harvesting by reducing the Debye length and strengthening the internal electric field [4].

As reflected in the photovoltaic parameters reported in Table 5, the highest power conversion efficiencies (η) for the $ZnTiO_3$-based device were 7.65%. While this value represents a favorable balance between donor states and deep traps within the explored

parameter space, it remains limited by the absorption-driven constraint on photocurrent generation. In this respect, the multilayer configuration should be considered a theoretical upper-bound scenario, illustrating the extent to which geometric effects can partially mitigate optical losses without altering the underlying electronic structure of the absorber.

The spectral response of the $ZnTiO_3$-based devices is illustrated in Figure 8, which compares the external quantum efficiency (EQE) of the monolayer and multilayer configurations. In the monolayer architecture, the EQE exhibits a rapid decline beyond the near-UV region, reflecting the limited absorption capability of $ZnTiO_3$ in the visible spectrum. This behavior is directly related to the material's indirect bandgap and its moderate absorption coefficient, which restricts efficient photogeneration to a relatively narrow wavelength range [6,29]. Consequently, carrier generation at longer wavelengths is significantly reduced, imposing a fundamental limitation on the achievable short-circuit current density. In contrast, the theoretical multilayer configuration shows a remarkably broader EQE response extending further into the visible region, indicating a higher probability of photon absorption across the device. The multilayer configuration represents an idealized scenario designed to explore the potential impact of geometric light-management strategies on $ZnTiO_3$-based devices. In this architecture, the absorber is redistributed into several sublayers, effectively increasing the optical path length without modifying the intrinsic electronic structure of the material. As a result, the probability of photon absorption within the device increases, partially compensating for the relatively low absorption coefficient characteristic of $ZnTiO_3$. It is important to emphasize that the higher projected efficiency obtained for the multilayer configuration does not arise from changes in the vacancy-induced electronic structure or from variations in the donor–trap equilibrium analyzed for the single-layer system. As shown in Table 5, the simulated efficiency exhibits only minor variations with the vacancy fraction within the explored range (θvo = 0.05–0.10%), indicating that the overall device performance is primarily controlled by the donor–trap balance rather than by the absolute vacancy concentration. The multilayer configuration was therefore evaluated under the defect-engineering conditions that yielded the best performance in the single-layer device, corresponding to a donor-dominated configuration (θ_D = 0.9 and θ_{tr} = 0.1) and a representative vacancy fraction of θvo = 0.07%. Under these conditions, the efficiency enhancement observed in the multilayer architecture originates mainly from the improved light harvesting enabled by thickness scaling and geometric redistribution of the absorber. By dividing the absorber into thinner sublayers, the effective optical path length increases while maintaining favorable carrier collection conditions [43]. Consequently, the multilayer configuration should be interpreted as a theoretical upper-bound scenario illustrating the maximum performance that $ZnTiO_3$ could achieve if its intrinsic optical limitations were partially mitigated through advanced device design, allowing geometric light-management effects to be distinguished from vacancy-induced electronic modifications.

Table 6 presents a comparative analysis of the devices presented in this study with established photovoltaic technologies.

Table 6. Comparison of the external quantum efficiency (EQE) of $ZnTiO_3$ with respect to other photovoltaic materials.

Solar Cell Type	Efficiency (%)	Reference
$ZnTiO_3$ perovskite single layer with VO	7.65	This work
$ZnTiO_3$ perovskite multilayer with VO	19.25	This work
Doped or nanomaterial-modified PSC	16.00	[18]
Advanced commercial PSC	25.60	[44]
PSC with deep molecular passivation	25.95	[44,45]
Inorganic PSC ($RbGeI_3$)	23.00	[14]

Table 6. *Cont.*

Solar Cell Type	Efficiency (%)	Reference
Hybrid halide-organic perovskite	25.05	[18]
Perovskite–Si tandem cells	29.50	[44,45]
Bifacial PERC/HJT cells	23.50	[43]
HIT/HJT cells	26.20	[43]
Amorphous silicon cells	11.00	[46]
Multicrystalline silicon cells	20.00	[47]
Monocrystalline silicon cells	23.50	[43]

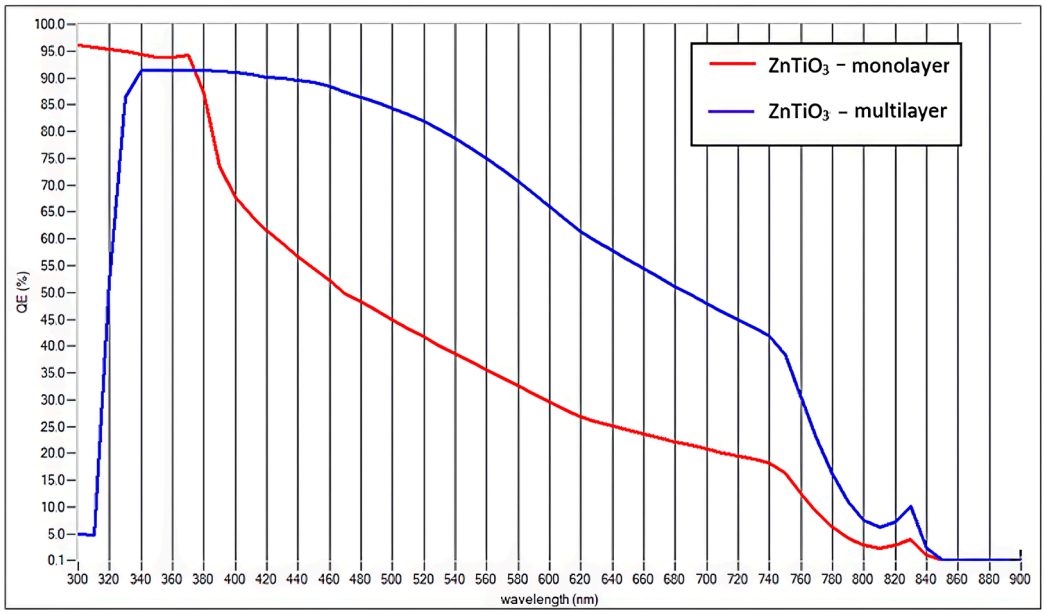

Figure 8. Variation of EQE for $ZnTiO_3$: multilayer and single layer.

As Table 6 shows, $ZnTiO_3$-based devices within the broader photovoltaic landscape, enabling a direct comparison with established technologies. While the single-layer configuration exhibits clearly limited efficiency (7.65%), the multi-layer architecture achieves projected values of 19.25% with an idealized thickness scaling (≈2 μm). At this level, $ZnTiO_3$ surpasses the typical efficiencies of amorphous silicon cells and approaches those of multicrystalline silicon technologies; however, it still falls short of the performance achieved by next-generation hybrid halide perovskites, perovskite-silicon tandem cells, and advanced heterojunction architectures. The superior efficiencies reported for these systems arise primarily from their direct or quasi-direct bandgap nature and substantially higher absorption coefficients, which enable efficient photogeneration across a broad spectral range using absorber layers that are approximately an order of magnitude thinner [48–50]. Furthermore, their more favorable charge transport properties and lower sensitivity to defect-mediated recombination facilitate the simultaneous achievement of high short-circuit current densities and open-circuit voltages [5]. Consequently, while multilayer structuring and vacancy engineering improve the performance of $ZnTiO_3$, its intrinsic optical limitations cannot be fully compensated for by thickness scaling or geometric light management strategies alone.

3. Materials and Methods

3.1. Computational Methodology

All electronic and structural calculations were performed using Density Functional Theory (DFT) as implemented in the Vienna Ab initio Simulation Package (VASP), version

6.2.1, developed by VASP Software GmbH in Vienna, Austria [51,52]. Molecular modeling and visualization were performed using BioVia Materials Studio, version 5.5, provided by BioVia in San Diego, CA, USA. The interaction between valence electrons and ionic cores was described using the projector augmented wave (PAW) method [53], while the exchange-correlation effects were treated within the generalized gradient approximation (GGA) employing the Perdew–Burke–Ernzerhof (PBE) functional [54,55]. The Kohn–Sham equations were solved self-consistently using a plane-wave basis set with a kinetic energy cutoff of 500 eV [56]. Structural optimizations were performed until the electronic self-consistency criterion reached and energy change below 10^{-5} eV and the residual Hellmann–Feynman forces were smaller than 0.005 eV·Å^{-1} [57]. Brillouin-zone integrations were conducted using the Monkhorst–Pack scheme [58], with k-point meshes adapted to each optimization stage; for slab geometries, the adequacy of the k-point sampling was then verified using k-gamma and k-spacing criteria.

Primitive cells were optimized using symmetric k-point meshes of 3 × 3 × 3 (cubic) and 3 × 2 × 1 (hexagonal). Slab models were then generated by applying a (101) crystallographic cut to both phases, introducing a vacuum region of 15 Å along the surface-normal direction. Selective dynamics were applied to the two outermost oxygen layers, and a 3 × 2 × 1 k-point mesh was employed for all slab calculations. The formation energy of a single neutral oxygen vacancy (F center) was evaluated at different surface and subsurface positions within the slab in order to identify the energetically most favorable configuration. Spin polarization and an initial magnetic moment distributed over the two Ti atoms neighboring the vacancy were considered [21]. Once the optimal vacancy configuration was identified, electronic-structure calculations were refined by incorporating the Hubbard on-site correction (+U). Different U values were examined, yielding an optimal combination of U = 5.00 eV for Ti and U = 7.25 eV for Zn [7].

3.2. Determination of Electronic and Optical Properties of $ZnTiO_3$

The electronic band structure was computed along high-symmetry paths in the reduced two-dimensional Brillouin zone (Γ–M–K–Γ) [30,59,60]. Total and partial densities of states (DOS and PDOS) were calculated to identify the orbital contributions of the valence and conduction bands, as well as to assess the impact of structural phase and defect formation on the electronic structure. The macroscopic electrostatic potential was extracted along the surface-normal direction to determine the vacuum reference level [61]. A linear correction was applied in the vacuum region to remove the residual slope, and the vacuum level was defined from the most stable plateau (right-hand side), ensuring a field-free reference [57,62,63]. Based on this corrected alignment, the electron affinity (χ) was calculated as the difference between the vacuum level and the conduction-band minimum referenced at the center of the slab [6]:

$$\chi = E_{vac} - E_{CB}^{center} \quad (1)$$

where E_{vac} represents the corrected vacuum level, defined as the planar-averaged electrostatic potential in the vacuum region after removal of the artificial slope, and E_{CB}^{center} denotes the conduction band minimum (CBM) in the central, bulk-like region of the slab, sufficiently far from both vacuum interfaces to avoid surface or electrostatic artifacts.

Optical properties such as dielectric permittivity (ε) were derived from the complex dielectric function obtained within the independent-particle approximation (IPA) [64]. Within this framework, microscopic local-field effects (LFE) were not explicitly included since their incorporation requires evaluation of the full microscopic dielectric matrix, which substantially increases the computational cost, particularly for large supercells and slab geometries containing defects, as those considered in the present study [65]. It is worth

noting that neglecting LFE within the IPA may influence the quantitative accuracy of the calculated dielectric response, especially in systems exhibiting strong microscopic charge inhomogeneity or reduced symmetry [66]. This limitation can be more pronounced in slab geometries, where the presence of vacuum interfaces and defect-induced charge redistribution may enhance local electrostatic variations near the surface [67]. Nevertheless, for wide-bandgap oxide semiconductors such as $ZnTiO_3$, the IPA framework can still provide useful qualitative insight into the optical response, including the approximate position of the absorption edge and the effect of defect-induced states on optical transitions. Consequently, the present optical model should be interpreted as providing a first-order approximation of the absorption behavior of defect-engineered $ZnTiO_3$ rather than a complete many-body description of its optical response [65]. On other hand, since slab geometries include a finite vacuum fraction that dilutes the dielectric response, a correction was applied based on the ratio between the slab thickness and the total supercell length along the surface-normal direction [68]. The effective high-frequency dielectric constant was extracted from the corrected out-of-plane component, $\varepsilon_{\infty,zz}$, which is appropriate for non-polar slab geometries [65].

3.3. Parameters for Photovoltaic Performance Evaluation

After establishing the electronic properties of $ZnTiO_3$, its photovoltaic performance was evaluated through device-level simulations using the one-dimensional Solar Cell Capacitance Simulator (SCAPS-1D), version 3.3.11 developed at Department of Electronics and Information Systems (ELIS) of the University of Gent, Belgium [16]. The simulations were performed under steady-state conditions by solving the coupled Poisson and carrier continuity equations within the drift–diffusion [16,69]. The electrostatic potential is obtained from Poisson's equation [29]:

$$\frac{d^2\psi(x)}{dx^2} = -\frac{q}{\varepsilon} \times \left[p(x) - n(x) + N_D^+(x) - N_A^-(x)\right] \quad (2)$$

where $\frac{d^2\psi(x)}{dx^2}$ represents the spatial curvature of the electrostatic potential, q and ε correspond to the elementary charge and the permittivity of the material, respectively, p and n refer to concentration of holes and electrons, respectively, and $N_D^+(x)$ and $N_A^-(x)$ denote the concentration of ionized donor and acceptor impurities, respectively. Carrier transport was described by continuity equations [29]:

$$\nabla \cdot J_n = q(G(x) - R(x)) \quad (3)$$

$$\nabla \cdot J_p = -q(G(x) - R(x)) \quad (4)$$

where $G(x)$ is the carrier generation, $R(x)$ is the carrier recombination rate (including trap-assisted channels intrinsic to the SRH-limited regime considered in this study), and J_n and J_p are the electron and hole drift–diffusion current densities, which are defined as [16]:

$$J_n = qn\mu_n E + qD_n \nabla n \quad (5)$$

$$J_p = qn\mu_p E - qD_p \nabla p \quad (6)$$

where μ_n and μ_p correspond to the mobility of electrons and hole, E is the electric field inside the material, ∇n and ∇p represent the spatial concentration gradient of electron and hole concentration, respectively, and D_n and D_p are the diffusion coefficient of electrons and holes.

Because the optical response directly determines the photogeneration rate and, consequently, the attainable short-circuit current density J_{SC}, the absorption coefficient was modeled using a hybrid analytical parametrization. The formulation combines an indirect Tauc-type onset for phonon-assisted transitions that is representative of pristine $ZnTiO_3$ and anchored to its characteristic UV absorption magnitude [2,70], with a Gaussian sub-gap contribution accounting for vacancy-induced intragap transitions, as defined by [71–73]:

$$\alpha_{total} = \frac{1}{t_{slab}} \int_0^{t_{slab}} \left[\alpha_{Tauc}(E, E_g(z)) + \alpha_{def}(E)\right] dz \quad (7)$$

where t_{slab} represents the thickness of the $ZnTiO_3$ absorber layer (300 nm), α_{Tauc} corresponds to the interband (band-to-band) absorption component, and α_{def} denotes the defect-induced absorption associated with centers F (oxygen vacancies).

The Tauc component follows the conventional quadratic energy dependence for indirect semiconductors and is implemented here in a scaled form to accommodate the selected broadening parameters [74,75]:

$$\alpha_{Tauc}\ \left(E, E_g(z)\right) = \frac{\alpha_{E04}}{(\Delta E)^2} \times (E - E_g(z))^2, E \geq E_g \quad (8)$$

where E denotes incident photon energy, and $E_g(z)$ represents the effective indirect optical bandgap of the material, which may vary with depth due to bandgap narrowing. The parameter ΔE is an energy scaling parameter introduced to control the effective amplitude of the indirect onset, such that $E_{04} = E_g + \Delta E$, and $\alpha_{E04} = 10^4\ cm^{-1}$ defines the calibration condition, ensuring that the absorption coefficient reaches the prescribed reference magnitude at the energy E_{04}. The prefactor therefore acts as an effective normalization term that enforces this amplitude constraint while preserving the quadratic energy dependence characteristic of indirect transitions. Notably, the value α_{E04} was adopted as the reference magnitude for pristine $ZnTiO_3$, in line with previously reported optical properties [6,70].

Oxygen vacancies introduce localized electronic states and modify the host electronic structure, producing defect-induced band-gap renormalization. Because the formation energy of oxygen vacancies increases with depth, their concentration is expected to decrease away from the surface, generating a defect-modulated region near the surface followed by a progressively bulk-like region as the thickness increases [7,76]. As a consequence, the magnitude of the defect-induced bandgap renormalization is not spatially uniform within the absorber layer, and the optical bandgap progressively approaches the pristine value at larger depths where the vacancy concentration becomes negligible. To represent this physical behavior in the optical absorption model, the bandgap was described as a depth-dependent function $E_g(z)$, assuming that the local band-gap renormalization scales with the local vacancy concentration. This formulation provides an effective description of the gradual transition between the defect-rich surface region and the bulk-like interior of the absorber. Accordingly, the bandgap variation along the depth was expressed as [37,77,78]:

$$E_g(z) = E_{g,0} - \Delta E_g^{BGN}(z) = E_{g,0} - BGN_{max}\left(\frac{C_{VO}(z)}{C_0}\right) \quad (9)$$

where $E_{g,0}$ denotes the pristine bandgap of $ZnTiO_3$ (i.e., in the absence of vacancies), and BGN_{max} represents the maximum band-gap reduction, defined as $BGN_{max} = E_{g,0} - E_{g,VO}$, with $E_{g,VO}$ corresponding to the bandgap at the vacancy-rich surface. The term $C_{VO}(z)$ describes the local concentration of oxygen vacancies, assumed to follow an exponential decay profile, which is in agreement with previously reported near-surface defect gradients [6,79]:

$$C_{VO}(z) = C_0 \times e^{-\frac{z}{L}} \quad (10)$$

Here, C_0 is the reference vacancy concentration, and L denotes the effective decay length that governs the spatial distribution of defects. In this study, L was set to 50 nm, defining the characteristic length scale over which the vacancy concentration decreases. Substituting Equation (10) into Equation (9) results in the cancellation of C_0, so that the band-gap renormalization depends solely on the characteristic ratio α/L and becomes independent of the absolute magnitude of the initial vacancy concentration.

On the other hand, to capture defect-enabled sub-gap absorption, the vacancy-related contribution was modeled as a Gaussian oscillator [75,80], given by the equation [81]:

$$\alpha_{def}(E) = \alpha_{max} \times \exp\left[-\frac{(E - E_0)^2}{2\sigma^2}\right] \quad (11)$$

where α_{max} represents the maximum amplitude of the defect-induced absorption, E_0 is the central energy of the gaussian oscillator and σ is the standard deviation (energy broadening parameter) of the Gaussian, which is mathematically related to the full width at half maximum (FWHM) through identity $\sigma = \frac{FWHM}{2.355}$. The center energy $E_0 = 0.85$ eV was selected to position the defect-enabled sub-gap absorption band in the near-infrared ($\lambda \approx 1.46$ μm), i.e., well below the intrinsic interband absorption edge of $ZnTiO_3$. This ensures that the added term captures weak intragap or defect-related transitions without distorting the band-edge fit. It is worth emphasizing that in optical dispersion modeling of defected oxide semiconductors, additional Gaussian oscillators are incorporated in the sub-eV regime (up to ~0.8 eV) to account for defect-induced sub-gap absorption features [82–84].

The peak magnitude of the defect-related Gaussian contribution was set to $\alpha_{max} = 5 \times 10^4$ cm^{-1}. This value maintains the physically meaningful sub-gap absorption while not exceeding the intrinsic interband absorption predicted by the Tauc model, whose maximum remains below 1×10^5 cm^{-1} in the present model. By restricting the defect-related amplitude to about half of the intrinsic maximum, the model maintains band-to-band absorption as the dominant optical process, while the Gaussian contribution simply extends absorption into the sub-gap region without redefining the absorption threshold. The Gaussian broadening parameter was defined as σ = 0.60 eV which corresponds to FWHM = 1.41 eV. This broadening falls within the range of Gaussian widths reported in optical dispersion studies of perovskite-type defected oxides and TiO_x, where FWHM values on the order of 1–2 eV are commonly used to reproduce distributed sub-gap absorption features [71,85]. In this study, vacancy concentrations on the order of 10^{-3} and 10^{-4} per lattice site were considered, corresponding to moderately high but non-degenerate defect densities. Such defect densities generate deep traps that lead to inhomogeneous energetic distributions resulting from local structural distortion, variations in coordination geometry, and defect–defect interactions [72,86,87]. Finally, a minimum optical background of 100 cm^{-1} was imposed to avoid non-physical vanishing absorption at the lowest energies [2,31].

Bulk and interface defect states were incorporated in the SCAPS simulations using a simplified Shockley–Read–Hall description, assuming neutral single-level traps with symmetric electron and hole capture cross-sections (Table 7). For all layers, bulk defect states were referenced with respect to the nearest band edge (below the conduction band for n-type layers and above the valence band for p-type layers), with characteristic energy offsets selected to represent shallow-to-intermediate recombination centers. In the $ZnTiO_3$ absorber, the modeled bulk defect does not explicitly correspond to oxygen vacancies but rather represents an effective distribution of intrinsic defects within the bulk that may act as shallow or deep SRH recombination centers [16,28].

Table 7. Modeling parameters for PSC layer defects.

Parameter	Spiro-OMeTAD [35]	FTO [36]	ZnO [33]	* $ZnTiO_3$ (Active Layer)
Defect type	Neutral	Neutral	Neutral	Neutral
Electron capture cross-section (cm^2)	1.0×10^{-15}	1.0×10^{-15}	1.0×10^{-15}	1.0×10^{-15}
Hole capture cross-section (cm^2)	1.0×10^{-15}	1.0×10^{-15}	1.0×10^{-15}	1.0×10^{-15}
Energy distribution	Single	Single	Single	Single
Reference for defect level (E_t)	Above EV	Below EC	Below EC	Below EC
Energy with respect to reference (eV)	0.400	0.100	0.400	0.400
Defect density (cm^{-3})	1.0×10^{14}	1.0×10^{14}	1.0×10^{14}	5×10^{13}

* The defect modeled for $ZnTiO_3$ does not correspond to oxygen vacancies, but rather to other defects that may be distributed within the bulk (forming shallow or deep SRH traps).

Interface defects were treated independently, with lower defect densities than in the bulk and energy levels positioned relative to the local band alignment at each interface, reflecting their role as non-ideal recombination sites rather than dominant transport-limiting centers (Table 8). The adopted defect densities and capture cross-sections were selected to ensure numerical stability and physical consistency, while allowing the recombination dynamics to be governed primarily by the absorber layer and its defect-mediated electronic structure.

Table 8. Modeling parameters for PSC interfaces.

Parameter	FTO/ETL [88]	ETL/$ZnTiO_3$ [88]	$ZnTiO_3$/HTL [69]
Defect type	Neutral	Neutral	Neutral
Electron capture cross-section (cm^2)	1.0×10^{-19}	1.0×10^{-19}	1.0×10^{-19}
Hole capture cross-section (cm^2)	1.0×10^{-19}	1.0×10^{-19}	1.0×10^{-19}
Energy distribution	Single	Single	Single
Reference for defect level (E_t)	Above middle of interface gap	Below the lowest EC	Above the highest EV
Energy with respect to reference (eV)	0.100	0.100	0.100
Defect density (cm^{-3})	1.0×10^{12}	1.0×10^{12}	1.0×10^{12}

4. Conclusions

This study demonstrated that perovskite-type $ZnTiO_3$, particularly in its hexagonal phase, exhibits superior structural stability relative to the cubic phase and preserves its crystalline integrity under controlled oxygen-vacancy formation. Density Functional Theory (DFT) calculations confirmed that neutral oxygen vacancies act predominantly as donor-like defects, inducing significant bandgap narrowing from approximately 2.96 eV to ~1.47 eV while maintaining the intrinsic indirect band-gap character of the material. Density-of-states analysis revealed the coexistence of shallow Ti-3d–derived donor states and deeper localized trap states, clarifying the dual role of vacancies in enhancing carrier density while simultaneously introducing recombination pathways.

From an optoelectronic standpoint, the combined Tauc–Gaussian absorption model consistently described the vacancy-induced extension of the absorption edge into the visible region. However, even under optimized vacancy fractions and absorber thickness, $ZnTiO_3$ retains a moderate absorption coefficient compared to direct-bandgap semiconductors, limiting the achievable photogeneration rate. SCAPS simulations within the FTO/ZnO/$ZnTiO_3$/Spiro-OMeTAD architecture showed that device performance is maximized within a narrow donor-dominated regime, yielding Voc ≈ 1.11 V, FF ≈ 83%, and a power conversion efficiency of approximately 7.65% for the single-layer configuration.

Importantly, the multilayer configuration explored in this work indicates that geometric and thickness-scaling strategies can substantially enhance the projected efficiency, approaching 19.25% under idealized conditions. While this value does not reach the per-

formance levels of state-of-the-art hybrid perovskites or tandem architectures, it places $ZnTiO_3$ within a technologically relevant efficiency window comparable to certain commercial silicon-based technologies. These findings suggest that, although intrinsic optical constraints associated with the indirect bandgap impose an upper performance limit, multilayer structuring and defect engineering enable $ZnTiO_3$ to approach moderate efficiency regimes without altering its fundamental electronic structure.

Overall, $ZnTiO_3$ does not emerge as a competitive high-efficiency absorber for single-junction photovoltaic applications in its current form. Nevertheless, its structural robustness, non-toxic composition, and tunable defect-mediated electronic properties indicate potential for alternative photovoltaic strategies, including multilayer or hybrid architectures where stability and defect tolerance are prioritized. Future experimental validation and advanced light-management designs will be essential to determine whether the theoretical upper-bound performance identified here can be realistically approached. In addition, more rigorous optical modeling incorporating many-body effects, such as excitonic interactions described within the Bethe–Salpeter framework, would allow a more accurate description of the optical spectra beyond the independent-particle approximation adopted in this work.

Supplementary Materials: The following supporting information can be downloaded at: https://www.mdpi.com/article/10.3390/ijms27062668/s1.

Author Contributions: Conceptualization, X.J.-F. and A.T.; methodology, X.J.-F. and A.T.; software, X.J.-F. and A.T.; validation, X.J.-F. and A.T.; formal analysis, X.J.-F. and A.T.; investigation, X.J.-F. and A.T.; resources, X.J.-F.; data curation, X.J.-F. and A.T.; writing—original draft preparation, A.T.; writing—review and editing, X.J.-F. and A.T.; visualization, X.J.-F. and A.T.; supervision, X.J.-F.; project administration, X.J.-F.; funding acquisition, X.J.-F. All authors have read and agreed to the published version of the manuscript.

Funding: The APC was funded by Universidad Técnica Particular de Loja, VIN-56.

Institutional Review Board Statement: Not applicable.

Informed Consent Statement: Not applicable.

Data Availability Statement: The original contributions presented in this study are included in the article and Supplementary Material. Further inquiries can be directed to the corresponding author.

Acknowledgments: The authors would like to thank the Universidad Técnica Particular de Loja (UTPL) for the computing time on the High-Performance Computing (HPC) server.

Conflicts of Interest: The authors declare no conflicts of interest.

Abbreviations

The following abbreviations are used in this manuscript:

DFT	Density Functional Theory
SCAPS	Solar Cell Capacitance Simulator
VASP	Vienna Ab initio Simulation Package
VO	Oxygen Vacancy
SRH	Shockley-Read-Hall Recombination
DOS	Density of states
PDOS	Projected Density of States
PSC	Perovskite Solar Cell
ETL	Electron Transport Layer
HTL	Hole Transport Layer
FTO	Fluorine-doped tin oxide
Spiro-OMeTAD	2,2′,7,7′-tetrakis(N,N-di-p-methoxyphenylamine)-9,9′-spirobifluorene
EQE	External Quantum Efficiency

GGA	Generalized Gradient Approximation
PBE	Perdew–Burke–Ernzerhof functional
IPA	Independent-particle approximation
LFE	Local-field effects
Eg	Bandgap energy
CBM	Conduction band minimum
VBM	Valence band maximum
ND	Donor density
Ntr	Trap density
Voc	Open-circuit voltage
Jsc	Short-circuit current density
FF	Fill factor
η	Power conversion efficiency

References

1. Gonzales, L.L.; da Silva Hartwig, M.; Fassbender, R.U.; Moreira, E.C.; Pereira, M.B.; Jardim, P.L.G.; Raubach, C.W.; Moreira, M.L.; da Silva Cava, S. Properties of Zinc Titanates Synthesized by Microwave Assisted Hydrothermal Method. *Heliyon* **2021**, *7*, e06521. [CrossRef]
2. Müllerová, J.; Šutta, P.; Medlín, R.; Netrvalová, M.; Novák, P. Optical Properties of Zinc Titanate Perovskite Prepared by Reactive RF Sputtering. *J. Electr. Eng.* **2017**, *68*, 10–16. [CrossRef]
3. Chen, W.Y.; Wang, C.P.; Chen, P.C.; Lin, K.Y.A.; Ghosh, S.; Huang, C.W.; Nguyen, V.H. Perovskite Zinc Titanate Photocatalysts Synthesized by the Sol–Gel Method and Their Application in the Photocatalytic Degradation of Emerging Contaminants. *Catalysts* **2021**, *11*, 854. [CrossRef]
4. Raju, T.D.; Murugadoss, V.; Nirmal, K.A.; Dongale, T.D.; Kesavan, A.V.; Kim, T.G. Advancements in Perovskites for Solar Cell Commercialization: A Review. *Adv. Powder Mater.* **2025**, *4*, 100275. [CrossRef]
5. Lin, L.; Jones, T.W.; Yang, T.C.J.; Duffy, N.W.; Li, J.; Zhao, L.; Chi, B.; Wang, X.; Wilson, G.J. Inorganic Electron Transport Materials in Perovskite Solar Cells. *Adv. Funct. Mater.* **2021**, *31*, 2008300. [CrossRef]
6. Ali, Z.; Ali, S.; Ahmad, I.; Khan, I.; Rahnamaye Aliabad, H.A. Structural and Optoelectronic Properties of the Zinc Titanate Perovskite and Spinel by Modified Becke–Johnson Potential. *Phys. B Condens. Matter* **2013**, *420*, 54–57. [CrossRef]
7. Wexler, R.B.; Gautam, G.S.; Stechel, E.B.; Carter, E.A. Factors Governing Oxygen Vacancy Formation in Oxide Perovskites. *J. Am. Chem. Soc.* **2021**, *143*, 13212–13227. [CrossRef] [PubMed]
8. Xiao-Chao, Z.; Cai-Mei, F.; Zhen-Hai, L.; Pei-De, H. Electronic Structures and Optical Properties of Ilmenite-Type Hexagonal $ZnTiO_3$. *Acta Phys. -Chim. Sin.* **2011**, *27*, 47–51. [CrossRef]
9. Jaramillo-Fierro, X.; González, S.; Medina, F. La-Doped $ZnTiO_3/TiO_2$ Nanocomposite Supported on Ecuadorian Diatomaceous Earth as a Highly Efficient Photocatalyst Driven by Solar Light. *Molecules* **2021**, *26*, 6232. [CrossRef] [PubMed]
10. Zhang, F.; Ma, W.; Guo, H.; Zhao, Y.; Shan, X.; Jin, K.; Tian, H.; Zhao, Q.; Yu, D.; Lu, X.; et al. Interfacial Oxygen Vacancies as a Potential Cause of Hysteresis in Perovskite Solar Cells. *Chem. Mater.* **2016**, *28*, 802–812. [CrossRef]
11. Serrano, S.; Duque, C.; Medina, P.; Stashans, A. Oxgen-Vacancy Defects in $PbTiO_3$ and $BaTiO_3$ Crystals: A Quantum Chemical Study. *Adv. Org. Inorg. Opt. Mater.* **2003**, *5122*, 287–294. [CrossRef]
12. Meyer, E.L.; Mvokwe, S.A.; Oyedeji, O.O.; Rono, N.; Agoro, M.A. Computational Study of Chalcogenide-Based Perovskite Solar Cell Using SCAPS-1D Numerical Simulator. *Materials* **2025**, *18*, 186. [CrossRef]
13. Klein, J.; Kampermann, L.; Mockenhaupt, B.; Behrens, M.; Strunk, J.; Bacher, G.; Klein, J.; Kampermann, L.; Bacher, G.; Mockenhaupt, B.; et al. Limitations of the Tauc Plot Method. *Adv. Funct. Mater.* **2023**, *33*, 2304523. [CrossRef]
14. Qin, Z.; Zhang, Y.; Guo, J. SCAPS Simulation and DFT Study of Ultra-Thin Lead-Free Perovskite Solar Cells Based on $RbGeI_3$. *Opt. Commun.* **2024**, *554*, 130187. [CrossRef]
15. Srivastava, P.; Sadanand; Rai, S.; Lohia, P.; Dwivedi, D.K.; Qasem, H.; Umar, A.; Akbar, S.; Algadi, H.; Baskoutas, S. Theoretical Study of Perovskite Solar Cell for Enhancement of Device Performance Using SCAPS-1D. *Phys. Scr.* **2022**, *97*, 125004. [CrossRef]
16. Burgelman, M.; Nollet, P.; Degrave, S. Modelling Polycrystalline Semiconductor Solar Cells. *Thin Solid Film.* **2000**, *361–362*, 527–532. [CrossRef]
17. Perdew, J.P.; Burke, K.; Ernzerhof, M. Generalized Gradient Approximation Made Simple. *Phys. Rev. Lett.* **1996**, *77*, 3865–3868. [CrossRef]
18. Shaikh, J.S.; Shaikh, N.S.; Sheikh, A.D.; Mali, S.S.; Kale, A.J.; Kanjanaboos, P.; Hong, C.K.; Kim, J.H.; Patil, P.S. Perovskite Solar Cells: In Pursuit of Efficiency and Stability. *Mater. Des.* **2017**, *136*, 54–80. [CrossRef]

19. Inaguma, Y.; Aimi, A.; Shirako, Y.; Sakurai, D.; Mori, D.; Kojitani, H.; Akaogi, M.; Nakayama, M. High-Pressure Synthesis, Crystal Structure, and Phase Stability Relations of a $LiNbO_3$-Type Polar Titanate $ZnTiO_3$ and Its Reinforced Polarity by the Second-Order Jahn-Teller Effect. *J. Am. Chem. Soc.* **2014**, *136*, 2748–2756. [CrossRef] [PubMed]
20. Jaramillo-Fierro, X.; Capa, L.F.; Medina, F.; González, S. Dft Study of Methylene Blue Adsorption on $ZnTiO_3$ and TiO_2 Surfaces (101). *Molecules* **2021**, *26*, 3780. [CrossRef]
21. Stashans, A. Defects in Titanates. *Int. J. Nanotechnol.* **2004**, *1*, 399–430. [CrossRef]
22. Wang, X.; Zhang, G.; Sun, Q.; Fei, Z.; Wang, Y. New Insight into Effects of Oxygen Vacancies on Crystal Structure and Electrical Properties of Barium Titanate Dielectric Ceramic. *J. Solid State Chem.* **2023**, *320*, 123859. [CrossRef]
23. Rusevich, L.L.; Tyunina, M.; Kotomin, E.A.; Nepomniashchaia, N.; Dejneka, A. The Electronic Properties of SrTiO3-δ with Oxygen Vacancies or Substitutions. *Sci. Rep.* **2021**, *11*, 23341. [CrossRef] [PubMed]
24. Li, J.; Wu, H.; Zhong, R.; Wang, Y.; Ye, S.; Zhao, H.; Yan, K.; Zhu, Y.; Hu, Z.; Xie, W.; et al. Quenching-Induced Oxygen Vacancy Engineering Boosts Photocatalytic Activities of $CaTiO_3$. *Appl. Surf. Sci.* **2024**, *670*, 160619. [CrossRef]
25. Shengqi, X.; Sanjun, F.; Lin, L.; Feihu, S. Preparation Method of Black Titanium Dioxide. CN Patent CN102249300A, 23 November 2011. Available online: https://patents.google.com/patent/CN102249300A/en (accessed on 12 March 2026).
26. Gaohui, D.; Yawen, H.; Xiang, B.; Qingmei, S.; Bingshe, X. Oxygen-Deficient Gray Zinc Oxide and Preparation Method and Application Thereof. CN Patent CN113582218A, 2 November 2021. Available online: https://patents.google.com/patent/CN113582218A/en (accessed on 12 March 2026).
27. Elangovan, H.; Barzilay, M.; Huang, J.; Liu, S.; Cohen, S.; Ivry, Y. Engineering Individual Oxygen Vacancies: Domain-Wall Conductivity and Controllable Topological Solitons. *ACS Nano* **2021**, *15*, 13380–13388. [CrossRef] [PubMed]
28. Shockley, W.; Read, W.T. Statistics of the Recombinations of Holes and Electrons. *Phys. Rev.* **1952**, *87*, 835. [CrossRef]
29. Smets, A.H.M.; Jäger, K.; Isabella, O.; Van Swaaij, P.A.C.M.M.; Zeman, M. *Solar Energy—The Physics and Engineering of Photovoltaic Conversion, Technologies and Systems*, 1st ed.; UIT Cambridge Ltd., Ed.; UIT Cambridge Ltd.: Cambridge, UK, 2016; ISBN 9781906860325.
30. Deilmann, T.; Rohlfing, M.; Thygesen, K.S. Optical Excitations in 2D Semiconductors. *Electron. Struct.* **2023**, *5*, 033002. [CrossRef]
31. Ruiz-Fuertes, J.; Winkler, B.; Bernert, T.; Bayarjargal, L.; Morgenroth, W.; Koch-Müller, M.; Refson, K.; Milman, V.; Tamura, N. Ferroelectric Soft Mode of Polar $ZnTiO_3$ Investigated by Raman Spectroscopy at High Pressure. *Phys. Rev. B* **2015**, *91*, 214110. [CrossRef]
32. Antwi, L.-O.; Huang, S. Defect State Dynamics in Lead-Free Perovskite Solar Cells for Enhanced Efficiency. *Int. J. Mater. Sci. Appl.* **2024**, *13*, 113–120. [CrossRef]
33. Sobayel, K.; Shahinuzzaman, M.; Amin, N.; Karim, M.R.; Dar, M.A.; Gul, R.; Alghoul, M.A.; Sopian, K.; Hasan, A.K.M.; Akhtaruzzaman, M. Efficiency Enhancement of CIGS Solar Cell by WS2 as Window Layer through Numerical Modelling Tool. *Sol. Energy* **2020**, *207*, 479–485. [CrossRef]
34. Akhtar, J.; Aamir, M.; Sher, M. Organometal Lead Halide Perovskite. *Perovskite Photovolt. Basic Adv. Concepts Implement.* **2018**, 25–42. [CrossRef]
35. Singh, N.; Agarwal, A.; Agarwal, M. Performance Evaluation of Lead–Free Double-Perovskite Solar Cell. *Opt. Mater.* **2021**, *114*, 110964. [CrossRef]
36. Rono, N.; Merad, A.E.; Kibet, J.K.; Martincigh, B.S.; Nyamori, V.O. A Theoretical Investigation of the Effect of the Hole and Electron Transport Materials on the Performance of a Lead-Free Perovskite Solar Cell Based on $CH_3NH_3SnI_3$. *J. Comput. Electron.* **2021**, *20*, 993–1005. [CrossRef]
37. Zhang, J.; Willis, J.; Yang, Z.; Sheng, Z.; Wang, L.S.; Lee, T.L.; Chen, L.; Scanlon, D.O.; Zhang, K.H.L. Direct Determination of Band-Gap Renormalization in Degenerately Doped Ultrawide Band Gap β-Ga_2O_3 Semiconductor. *Phys. Rev. B* **2022**, *106*, 205305. [CrossRef]
38. Abbas, M.; Xu, X.; Rauf, M.; Kyaw, A.K.K. A Comprehensive Review on Defects-Induced Voltage Losses and Strategies toward Highly Efficient and Stable Perovskite Solar Cells. *Photonics* **2024**, *11*, 87. [CrossRef]
39. Wenderott, J.K.; Billo, T.; Fong, D.D. Epitaxial Oxide Ionotronics: Interfaces and Oxygen Vacancies. *APL Mater.* **2024**, *12*, 50901. [CrossRef]
40. Lee, S.; Jeon, J.; Lee, H. Probing Oxygen Vacancy Distribution in Oxide Heterostructures by Deep Learning-Based Spectral Analysis of Current Noise. *Appl. Surf. Sci.* **2022**, *604*, 154599. [CrossRef]
41. Labouret, A.; Villoz, M. *Solar Photovoltaic Energy*; The Institution of Engineering and Technology (IET): Stevenage, UK, 2010; pp. 1–373. [CrossRef]
42. Qian, J.; He, J.; Zhang, Q.; Zhu, C.; Chen, S.; Wei, Z.; Leng, X.; Zhou, Z.; Shen, B.; Peng, Y.; et al. Minimizing Interfacial Energy Losses in Inverted Perovskite Solar Cells by a Dipolar Stereochemical 2D Perovskite Interface. *J. Energy Chem.* **2023**, *90*, 496–503. [CrossRef]
43. Ling, Z.P. Effective Light Management in Thin Silicon Wafers. In *Advances in Silicon Solar Cells*; Springer: Cham, Switzerland, 2018; pp. 1–24. [CrossRef]

44. Zhang, P.; Li, M.; Chen, W.C. A Perspective on Perovskite Solar Cells: Emergence, Progress, and Commercialization. *Front. Chem.* **2022**, *10*, 802890, Erratum in *Front Chem.* **2025**, *13*, 1562415. [CrossRef]
45. Zhang, X. High-Efficiency Perovskite Solar Cells: Progress and Prospects. *E3S Web Conf.* **2024**, *553*, 01014. [CrossRef]
46. Schiff, E.A.; Hegedus, S.; Deng, X. Amorphous Silicon-Based Solar Cells. *Handb. Photovolt. Sci. Eng.* **2011**, 487–545. [CrossRef]
47. Zaidi, S.H. Crystalline Silicon Solar Cells: Carbon to Silicon—A Paradigm Shift in Electricity Generation. In *Crystalline Silicon Solar Cells*; Springer: Cham, Switzerland, 2021; Volume 1, pp. 1–258. [CrossRef]
48. Afre, R.A.; Pugliese, D. Perovskite Solar Cells: A Review of the Latest Advances in Materials, Fabrication Techniques, and Stability Enhancement Strategies. *Micromachines* **2024**, *15*, 192. [CrossRef]
49. Salem, M.S.; Okil, M.; Shaker, A.; Albaker, A.; Alturki, M. Design of N-i-p and p-i-n Sb_2Se_3 Solar Cells: Role of Band Alignment. *J. Phys. Energy* **2023**, *5*, 045007. [CrossRef]
50. Ünlü, F.; Jung, E.; Öz, S.; Choi, H.; Fischer, T.; Mathur, S. Chemical Processing of Mixed-Cation Hybrid Perovskites: Stabilizing Effects of Configurational Entropy. In *Perovskite Solar Cells: Materials, Processes, and Devices*; Wiley: Hoboken, NJ, USA, 2021; pp. 1–31. [CrossRef]
51. Kresse, G.; Furthmüller, J. Efficient Iterative Schemes for Ab Initio Total-Energy Calculations Using a Plane-Wave Basis Set. *Phys. Rev. B Condens. Matter Mater. Phys.* **1996**, *54*, 11169–11186. [CrossRef]
52. Wang, V.; Xu, N.; Liu, J.C.; Tang, G.; Geng, W.T. VASPKIT: A User-Friendly Interface Facilitating High-Throughput Computing and Analysis Using VASP Code. *Comput. Phys. Commun.* **2021**, *267*, 108033. [CrossRef]
53. Zhang, B.; Ma, X.; Zhu, H.Y.; Luan, C.; Xiao, H.; Ma, J.; Ma, J. Hexagonal $ZnTiO_3$ Single-Crystalline Films on α-Al_2O_3 Substrates: Structural and Photoelectric Properties. *J. Alloys Compd.* **2024**, *1008*, 176757. [CrossRef]
54. Sujith, C.P.; Joseph, S.; Mathew, T.; Mathew, V. First-Principles Investigation of Structural, Electronic and Optical Properties of Quasi-One-Dimensional Barium Cadmium Chalcogenides Ba2CdX3 (X = S, Se, Te) Using HSE06 and GGA-PBE Functionals. *J. Phys. Chem. Solids* **2022**, *161*, 110488. [CrossRef]
55. Haro, A.F. Generalized Gradient Approximation Made Simple: Theoretical Review: Aproximación Generalizada Del Gradiente Simplificada: Revisión Teórica. *Multidiscip. Lat. Am. J. (MLAJ)* **2025**, *3*, 1–7. [CrossRef]
56. Kohn, W.; Sham, L.J. Quantum Density Oscillations in an Inhomogeneous Electron Gas. *Phys. Rev.* **1965**, *137*, A1697. [CrossRef]
57. Falun, P.; Ngamwongwan, L.; Singsen, S.; Chotsawat, M.; Komen, P.; Junkaew, A.; Suthirakun, S. Enhancing V_2O_5 Cathode Performance through Heterostructure Engineering with the Ti3C2O2 MXene: A Computational Study. *J. Phys. Chem. C* **2024**, *128*, 10774–10783. [CrossRef]
58. Monkhorst, H.J.; Pack, J.D. Special Points for Brillouin-Zone Integrations. *Phys. Rev. B* **1976**, *13*, 5188–5192. [CrossRef]
59. Michel, K.H.; Verberck, B. Theory of Rigid-Plane Phonon Modes in Layered Crystals. *Phys. Rev. B* **2012**, *85*, 094303. [CrossRef]
60. Deilmann, T.; Thygesen, K.S. Finite-Momentum Exciton Landscape in Mono- and Bilayer Transition Metal Dichalcogenides. *2D Mater.* **2019**, *6*, 035003. [CrossRef]
61. Li-Sha, M.; Qian-Cheng, Z.; Lin, C.; Li-Sha, M.; Qian-Cheng, Z.; Lin, C. First-Principles Calculations on Electronic Structures of Zn Adsorbed on the Anatase TiO_2 (101) Surface Having Oxygen Vacancy and Hydroxyl Groups. *Acta Phys. Sin.* **2013**, *62*, 187101. [CrossRef]
62. Zhang, T.; Guo, H.; Shen, J.; Liang, Y.; Fan, H.; Jiang, W.; Wang, Q.; Tian, X.; Zhang, T.; Guo, H.; et al. Tunable Schottky Barriers and Magnetoelectric Coupling Driven by Ferroelectric Polarization Reversal of Mn3In2Se3 Multiferroic Heterostructures. *npj Comput. Mater.* **2024**, *10*, 238. [CrossRef]
63. Wang, T.; Oba, F. Slab Surface Passivation and Its Application to Band Offset Calculations for Polar Heterointerfaces of Zinc-Blende Semiconductors. *Phys. Rev. Mater.* **2023**, *7*, 084602. [CrossRef]
64. Gajdoš, M.; Hummer, K.; Kresse, G.; Furthmüller, J.; Bechstedt, F. Linear Optical Properties in the Projector-Augmented Wave Methodology. *Phys. Rev. B* **2006**, *73*, 045112. [CrossRef]
65. Yang, G.; Fan, J.; Gao, S.P. Momentum and Thickness Dependent Excitonic and Plasmonic Properties of 2D H-BN and MoS_2 Restored from Supercell Calculations. *Nanoscale Adv.* **2023**, *5*, 6990–6998. [CrossRef] [PubMed]
66. Wei, Y.; Shen, Y.R. Interfacial Local Field and Surface Response Coefficients. *J. Chem. Phys.* **2024**, *161*, 124117. [CrossRef]
67. Schwarz, K.; Sundararaman, R. The Electrochemical Interface in First-Principles Calculations. *Surf. Sci. Rep.* **2020**, *75*, 100492. [CrossRef]
68. Laturia, A.; Van de Put, M.L.; Vandenberghe, W.G. Dielectric Properties of Hexagonal Boron Nitride and Transition Metal Dichalcogenides: From Monolayer to Bulk. *npj 2D Mater. Appl.* **2018**, *2*, 6, Correction in *npj 2D Mater.* **2020**, *4*, 28. [CrossRef]
69. Haidari, G. Comparative 1D Optoelectrical Simulation of the Perovskite Solar Cell. *AIP Adv.* **2019**, *9*, 085028. [CrossRef]
70. Saritha, M.V.; Dastagiri, S.; Lakshmaiah, M.V.; Kumar, V.R.; Supriya, K.E.; Pakardin, G. Structural and Optical Properties of $ZnTiO_3$ Nanoparticles Synthesized by Hydrothermal Method. *Int. J. Eng. Res. Technol.* **2022**, *11*, 85–90. [CrossRef]
71. Enea, N.; Ion, V.; Viespe, C.; Constantinoiu, I.; Buiu, O.; Romanitan, C.; Scarisoreanu, N.D. Laser Processed Hybrid Lead-Free Thin Films for SAW Sensors. *Materials* **2022**, *15*, 8452. [CrossRef] [PubMed]
72. Strand, J.; Shluger, A.L. On the Structure of Oxygen Deficient Amorphous Oxide Films. *Adv. Sci.* **2024**, *11*, 2306243. [CrossRef]

73. Tumusange, M.S.; Bhandari, G.B.; Romestan, Z.; Uprety, P.; Subedi, I.; Romero, A.H.; Holcomb, M.B.; Podraza, N.J. Interpretation of Complex Optical Properties and Optical Transitions of Epitaxial LaMnO3 Thin Films. *Appl. Surf. Sci.* **2024**, *670*, 160682. [CrossRef]
74. Fox, M. *Luminescence Centres*, 2nd ed.; Oxford University Press, Ed.; Oxford University Press: New York, NY, USA, 2010; ISBN 9780199573363.
75. Budai, J.; Hanyecz, I.; Szilágyi, E.; Tóth, Z. Ellipsometric Study of SixC Films: Analysis of Tauc–Lorentz and Gaussian Oscillator Models. *Thin Solid Film.* **2011**, *519*, 2985–2988. [CrossRef]
76. Ahn, Y.N. The Effect of Oxygen Vacancies on the Diffusion Characteristics of Zn(II) Ions in the Perovskite $SrTiO_3$ Layer: A Computational Study. *Materials* **2023**, *16*, 3957. [CrossRef]
77. Bendaoudi, L.; Ouahrani, T.; Daouli, A.; Rerbal, B.; Boufatah, R.M.; Morales-García, A.; Franco, R.; Bedrane, Z.; Badawi, M.; Errandonea, D. Electronic and Electrocatalytic Properties of $PbTiO_3$: Unveiling the Effect of Strain and Oxygen Vacancy. *Dalton Trans.* **2023**, *52*, 11965–11980. [CrossRef]
78. Kim, J.Y.; Jin, M.J.; Hou, B.; Kim, M.P.; Um, D.S.; Kim, C. Il Reducing the Oxygen Vacancy Concentration in $SrTiO_3$-δ Thin Films via an Optimized O2 Plasma Treatment for Enhancing Device Properties. *Appl. Surf. Sci.* **2023**, *639*, 158271. [CrossRef]
79. Kler, J.; Börgers, J.M.; De Souza, R.A.; Kler, J.; Börgers, J.M.; De Souza, R.A. Surface Space-Charge Potential and Oxygen Surface Exchange Coefficient of $SrTiO_3$: The Effect of Surface Orientation. *Adv. Mater. Interfaces* **2023**, *10*, 2201434. [CrossRef]
80. Bohórquez, C.; Bakkali, H.; Delgado, J.J.; Blanco, E.; Herrera, M.; Domínguez, M. Spectroscopic Ellipsometry Study on Tuning the Electrical and Optical Properties of Zr-Doped ZnO Thin Films Grown by Atomic Layer Deposition. *ACS Appl. Electron. Mater.* **2022**, *4*, 925–935. [CrossRef]
81. Chen, L.; Li, Q.; Li, J.; Shan, Q. Advanced Optical Characterization of Multilayer Lead Zirconate Titanate Films: A Spectroscopic Ellipsometry Approach. *J. Appl. Phys.* **2025**, *138*, 094103. [CrossRef]
82. Avci, N.; Smet, P.F.; Poelman, H.; Van De Velde, N.; De Buysser, K.; Van Driessche, I.; Poelman, D. Characterization of TiO_2 Powders and Thin Films Prepared by Non-Aqueous Sol-Gel Techniques. *J. Solgel Sci. Technol.* **2009**, *52*, 424–431. [CrossRef]
83. Sahoo, S.S.; Mansingh, S.; Babu, P.; Parida, K. Black Titania an Emerging Photocatalyst: Review Highlighting the Synthesis Techniques and Photocatalytic Activity for Hydrogen Generation. *Nanoscale Adv.* **2021**, *3*, 5487–5524. [CrossRef]
84. Muthukrishnan, S.; Vidya, R.; Sjåstad, A.O. Band Gap Engineering of Anatase TiO_2 by Ambipolar Doping: A First Principles Study. *Mater. Chem. Phys.* **2023**, *299*, 127467. [CrossRef]
85. Morris, B.S.; Shayegan, Z.; Koch, D.; Palpant, B.; Chaker, M. Developing an Analysis Procedure and Dispersion Model for Pristine and W-Doped VO2 Thin Films Using Density Functional Theory and Spectroscopic Ellipsometry. *ACS Appl. Mater. Interfaces* **2024**, *16*, 68621–68631. [CrossRef] [PubMed]
86. Böer, K.W.; Pohl, U.W. Optical Properties of Defects. *Semicond. Phys.* **2023**, *2*, 703–753. [CrossRef]
87. Tripathy, S.R.; Baral, S.S. Defect Engineering in Semiconductor Photocatalysts: Enhancing Photocatalytic Activity for Green Energy Production. *Adv. Energy Sustain. Res.* **2025**, *6*, 2500110. [CrossRef]
88. Li, X.; Fang, Y.; Zhao, J. Optimizing Inorganic $Cs_4CuSb_2Cl_{12}/Cs_2TiI_6$ Dual-Absorber Solar Cells: SCAPS-1D Simulations and Machine Learning. *Nanomaterials* **2025**, *15*, 1245. [CrossRef] [PubMed]

Disclaimer/Publisher's Note: The statements, opinions and data contained in all publications are solely those of the individual author(s) and contributor(s) and not of MDPI and/or the editor(s). MDPI and/or the editor(s) disclaim responsibility for any injury to people or property resulting from any ideas, methods, instructions or products referred to in the content.